MICROCOPY RESOLUTION TEST CHART
NATIONAL BUREAU OF STANDARDS-1963-A

AD-A158 127

REPORT DOCUMENTATION PAGE

READ INSTRUCTIONS
BEFORE COMPLETING FORM

1. REPORT NUMBER	2. GOVT ACCESSION NO	3. RECIPIENT'S CATALOG NUMBER

4. TITLE (and Subtitle) Fusion Welding Research	5. TYPE OF REPORT & PERIOD COVERED 4th Annual Technical Report April 30, 1984
	6. PERFORMING ORG. REPORT NUMBER

7. AUTHOR(s) T. W. Eagar, G. B. Hunter, G. J. Dunn, C. D. Sorensen, M. L. Lin, D. E. Ries, C. D. Allemand, A. O. Oladipupo, A. Block-Bolten, R. Schoeder, K. T. Ulrich, N. S. Tsai	8. CONTRACT OR GRANT NUMBER(s) N00014-80-C-0384

9. PERFORMING ORGANIZATION NAME AND ADDRESS Department of Materials Science & Engineering Massachusetts Institute of Technology Cambridge, MA 02139	10. PROGRAM ELEMENT, PROJECT, TASK AREA & WORK UNIT NUMBERS

11. CONTROLLING OFFICE NAME AND ADDRESS Dr. Bruce A. MacDonald Office of Naval Research 800 N. Quincy, Arlington, VA 22217	12. REPORT DATE April 30, 1984
	13. NUMBER OF PAGES 121

14. MONITORING AGENCY NAME & ADDRESS(if different from Controlling Office)	15. SECURITY CLASS. (of this report) Unclassified
	15a. DECLASSIFICATION/DOWNGRADING SCHEDULE

16. DISTRIBUTION STATEMENT (of this Report)

Reproduction in whole or in part is permitted for any purposes of the
United States Government. Distribution of this document is unlimited.

17. DISTRIBUTION STATEMENT (of the abstract entered in Block 20, if different from Report)

18. SUPPLEMENTARY NOTES

19. KEY WORDS (Continue on reverse side if necessary and identify by block number)

20. ABSTRACT (Continue on reverse side if necessary and identify by block number)

This report summarizes progress during the fourth year of research on the
physics of arc welding processes. Studies include vapor emission from weld
pools, development of a high speed infrared temperature monitor, digital
signal analysis of weld noise voltages, convection and surface depression
of the weld pool, pulsed current gas metal arc welding of titanium, contact
tip wear in gas metal arc welding of titanium, fracture toughness of TY-80
weldments, and sensitization of 304 stainless steel welds.

DD FORM 1473 EDITION OF 1 NOV 65 IS OBSOLETE
1 JAN 73
S/N 0102-014-6601 |

FUSION WELDING RESEARCH

by

T. W. Eagar, G. B. Hunter, G. J. Dunn, C. D. Sorensen
M. L. Lin, D. E. Ries, C. D. Allemand, A. O. Oladipupo,
A. Block-Bolten, R. Schoeder, K. T. Ulrich, N. S. Tsai

Fourth Annual Technical Report

Contract N00014-80-C-0384

to

Office of Naval Research

Department of the Navy

Arlington, VA 22217

Attention: Dr. Bruce B. MacDonald

April 30, 1984

85   8   10   059

Table of Contents

ABSTRACT

Research studies on

This report summarizes progress during the fourth year of research on the physics of arc welding processes. ~~Studies~~ include: vapor emission from weld pools; development of a high speed infrared temperature monitor; digital signal analysis of weld noise voltages; convection and surface depression of the weld pool; pulsed current gas metal arc welding of titanium; contact tip wear in gas metal arc welding of titanium; fracture toughness of HY-80 weldments; and sensitization of 304 stainless steel welds. *Keywords: Spectrographic studies; Heavy section titanium; HY-80 weld metal; Sensors for arc welding automation.*

I. INTRODUCTION

This report describes work performed in the MIT Welding Laboratory under Office of Naval Research sponsorship. The work is generally fundamental in nature, but attempts have been made to interface the studies with specific U. S. Navy programs. The best example of the directed programs include evaluation of the fracture toughness of HY-80 weld metal.

The research conducted from 15 February 1983 to 15 February 1984 can broadly be divided into four main topics, viz.;

1. Spectrographic studies of the weld pool
2. Welding of heavy section titanium
3. Fracture toughness of HY-80 weld metal
4. Sensors for automation of arc welding

II. SPECTROSCOPY OF ARC WELDING

Spectroscopic studies of the arc welding process performed during the past contract year include development of a Multichannel Infrared-Red Temperature Micro-Analyzer, and a study of vapor emission from the weld pool. These two studies are coupled through a thermodynamic upper-bound analysis which has been published previously (1), and was expanded in a recent technical paper (see Appendix A). A brief description of the results of the experimental work is given below.

A. Vapor Emission from the Weld Pool

Mr. G. J. Dunn

Metal vapors in gas tungsten welding arcs are being studied in order to determine the effects of these vapors on arc properties and, subsequently, on weld bead configuration. Emission spectroscopy and monochromatic photography were used to determine the composition and distribution of vapors in arcs on stainless steels as previously reported (2).

Based on the experimental work, theoretical calculations have been made to study the effects of small additions of aluminum and calcium vapors on the electrical and thermal conductivities of argon and helium plasmas containing iron vapor. It was shown that, when an inert gas containing other metal vapors is considered rather than a pure inert gas, the effects of low ionization potential elements is far less significant than previous reports have found. It has been concluded that the effects of these minor elements on arc properties is probably of secondary importance in explaining variable weld penetration. Other effects, such as changes in the surface tension coefficient of the weld pool, may be more important in explaining the poor penetration observed in base metals containing these elements.

However, the effects of elements emitted by the tungsten electrode may be very significant, as the inert gas is otherwise free of contaminants in the upper region of the arc. In this case, the simple binary composition plasma model is valid, and the dramatic effects of even very small amounts of metal vapor on the arc transport properties may significantly alter the transport of energy to the weldment. This project is continuing and a thesis detailing the experimental and theoretical work will be completed in the next reporting period.

B. Infrared Measurement of the Weld Pool Surface Temperatures
Mr. G. B. Hunter

Experimental problems continue to plague this project. However, temperature measurements have been successfully made on solid targets using the equipment and new techniques developed for this study. The basic approach involves measuring the spectral radiance at approximately 200 wavelengths, using a multichannel detector. A Planck radiation law curve, assuming only that a smooth function exists between spectral emissivity and wavelength, is fitted to the spectral radiance vs. wavelength data to determine the temperature and spectral emissivity. This is a new method of spectrometric temperature measurement that has never been proposed elsewhere. A Multi-channel Infrared-Red Temperature Micro-Analyzer (MIRTMA) system has been developed using this technique. The basic procedure has been described previously (2).

Many of the problems encountered in this work have centered on the detector. An attempt to improve the MIRTMA was made by coupling an S1 photo-cathode proximity focused image tube to the S20 photocathode Silicon Intensified Target (SIT) detector. This proved unsatisfactory, however, because of internal

reflections occurring in the face plate of the tube, near field glare within the tube, and the production by the photocathode of bright spot artifacts in the image. Even without the tube, the SIT detector has various nonlinearities in its signal response to radiation intensity, not all of which have been corrected to allow an accurate calibration.

Despite the experimental difficulties, temperatures have been measured in a blackbody furnace from 1100 - 1273 K to within 1% of the furnace settings with a temporal resolution of 3 s and a spatial resolution of 0.1 mm. Work is now continuing to measure surface temperatures of a resistively heated platinum strip with unknown spectral emissivity values. This work will be included in a thesis that will be completed in the next reporting period.

III.   WELDING OF HEAVY SECTION TITANIUM

Joining of heavy section titanium is of particular concern to the Navy for advanced systems. During the past year, studies have continued on pulsed current gas metal arc welding and have commenced on contact tip wear in gas metal arc welding of titanium.

A.   Pulsed Current Gas Metal Arc Welding of Titanium

During the past year, this work has produced one thesis, the abstract for which is in Appendix B, and one technical paper which is included in Appendix C. The paper describes the technique of using laser backlighting to produce high speed movies of metal transfer during the welding process. This project is currently being postponed until another interested student can be found to continue this work.

B.   Contact Tip Wear in Gas Metal Arc Welding of Titanium

Copper contact tips wear very rapidly when titanium electrodes are used in gas metal arc welding. The goals of this project are to identify the mechanisms causing the increased wear and to find methods to reduce the wear. This work has produced one thesis to date. The abstract of this thesis is included in Appendix D. Work is continuing on this project and another thesis is expected to be completed soon.

IV. FRACTURE TOUGHNESS OF HY-80 WELDMENTS

Mr. A. O. Oladipupo

One project has been continued in this area. It involved investigation into metallurgical factors influencing charpy energy of submerged arc welded HY-80 steel. The abstract for a thesis discussing this work is included in Appendix E. Further work is being carried out to investigate the effects of retained austenite and nitrogen content on weld metal toughness of HY-80 steel weld plates.

V.   AUTOMATION OF WELDING

Automation is one area of welding technology that promises to pay tremendous dividends if high sensitivity, rugged sensors can be developed. One possible sensor is the arc itself, which is known to respond to geometric and chemical discontinuities at frequencies up to 20 kHz. In one study we are using digital signal analysis to measure these responses. In a second effort, the effects of surface depression and convection on weld pool shape and defect formation are being studied. These latter topics are of great importance in developing processes capable of producing weld pools of desired size and quality.

A.   Signal Analysis of Welding Noise Voltage

Mr. C. D. Sorenson

One of the major challenges of signal processing is the extraction of the important features from the spectrum of the system, which can be very noisy and thus tends to mask these important features. During the past contract period, our efforts to refine and improve our signal processing capabilities, such that we can identify the formation of welding defects, has proceeded in three areas: refinement of signal processing methods, use of a new high-speed A/D converter, and investigation of various current waveforms. The improvements made in each of these areas are discussed below.

In an effort to improve our ability to identify weld defects as they occur, we have refined and tested our signal processing methods. Among other things, we have altered our analysis so that it includes the input (current) waveform as well as the output (voltage) waveform. We have also performed a sensitivity analysis to determine the minimum size oscillations in the weld pool which can be detected.

The analysis which was used previously on the weld signals (3) assumed that the input current to the arc-puddle system was well known, or at least constant. Thus, only the output voltage was examined in an attempt to detect defects. This meant that any change in the input of which we were unaware would appear to be a change in the electrical characteristics of the arc. Therefore, it was necessary to eliminate the effects of minor variations in the input by using signal processing techniques which measure both the input and the output of a system. The functions which we chose are the frequency response function and the coherence function (4). These functions provide two important capabilities. First, they include both input and output information, and thus are able to separate the effects due to changes in the arc from changes in the input. Secondly, they provide a measure of the degree of correlation between input and output, and thus help us to determine whether the information which we are receiving is valid information or merely spurious noise. Figures 1 and 2 show the input and output spectra which are combined to yield a gain and phase function along with a coherence function. Although it is not proven conclusively, it is hypothesized that the peak shown at near 400 Hz is indicative of a weld puddle oscillation.

In addition to changing the method of measuring the arc system, a study has been made to determine the sensitivity of our analysis technique to changes in arc voltage or arc length, as would occur in an up-and-down puddle oscillation. A sinusoid of various amplitudes was summed onto the voltage from a weld in order to observe the changes in the system transfer function. Figure 3 shows the gain function for three such experiments. The amplitude of the imposed sine wave was 1%, 0.3% and 1.1% of the average arc voltage in figures 3a, 3b, and 3c respectively. Note the ability to easily observe the peak for the sinusoid in the 0.3% disturbance, and the visible peak even at 0.1%.
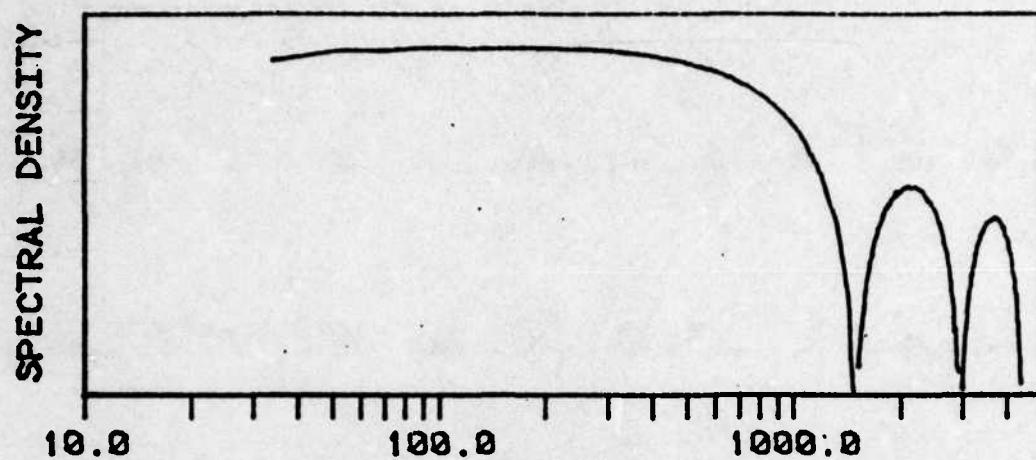
INPUT AUTOSPECTRUM
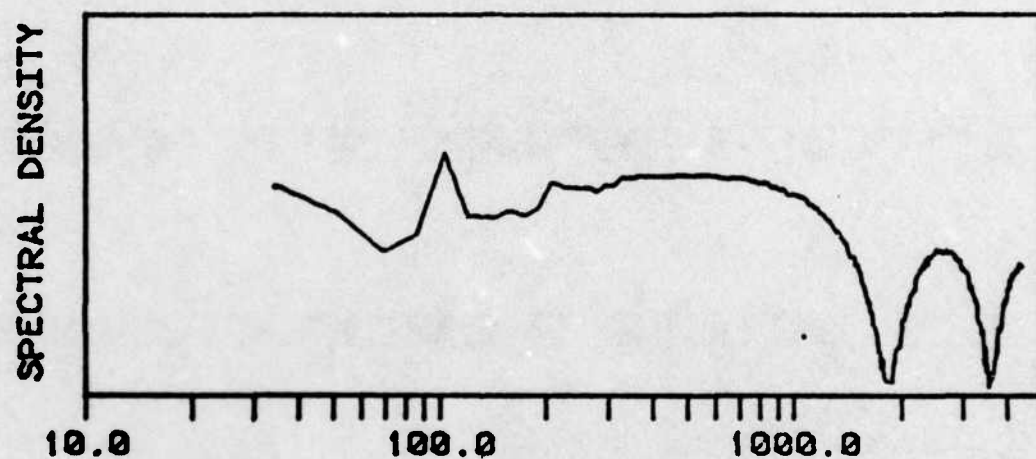
OUTPUT AUTOSPECTRUM
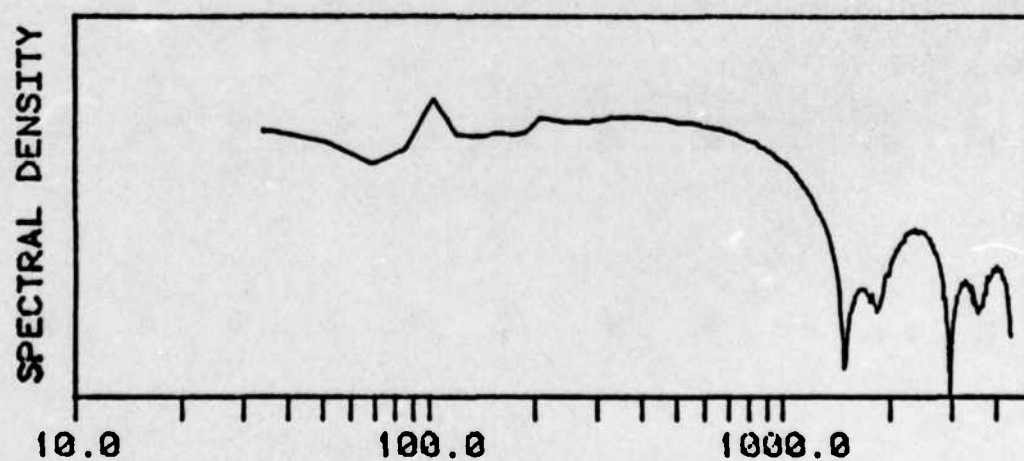
FREQUENCY, HZ.

CROSS SPECTRUM

Figure 1: Systems Spectra

COHERENCE FUNCTION

GAIN FACTOR

PHASE FACTOR

Figure 2: System Identification Functions

(a)   Sine wave amplitude of 1% of arc voltage

(b)   Sine wave amplitude of 0.3% of arc voltage.

(c) Sine wave amplitude of 0.1% of arc voltage.

Figure 3.   Gain plots for a weld signal with a 400 Hz sine wave imposed.

These results indicate that we should be able to observe puddle oscillations in the welding arc.

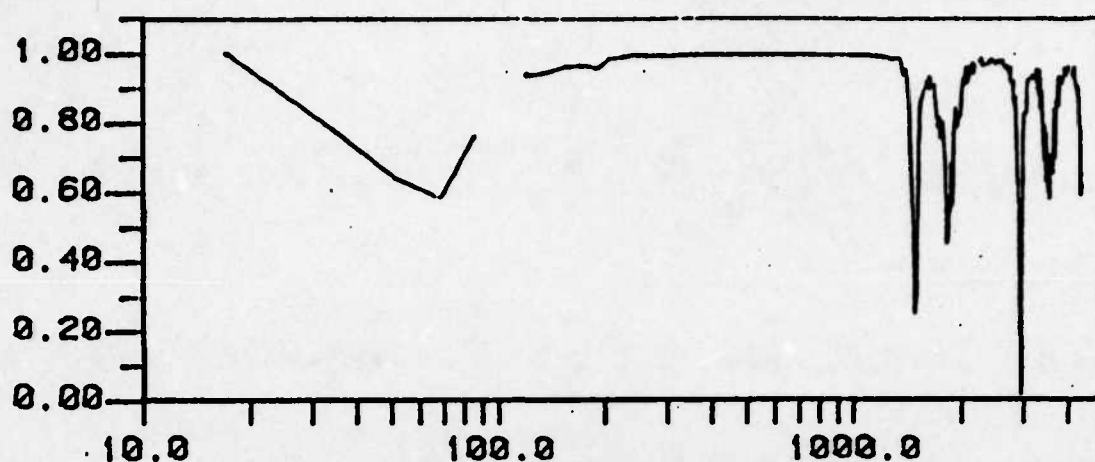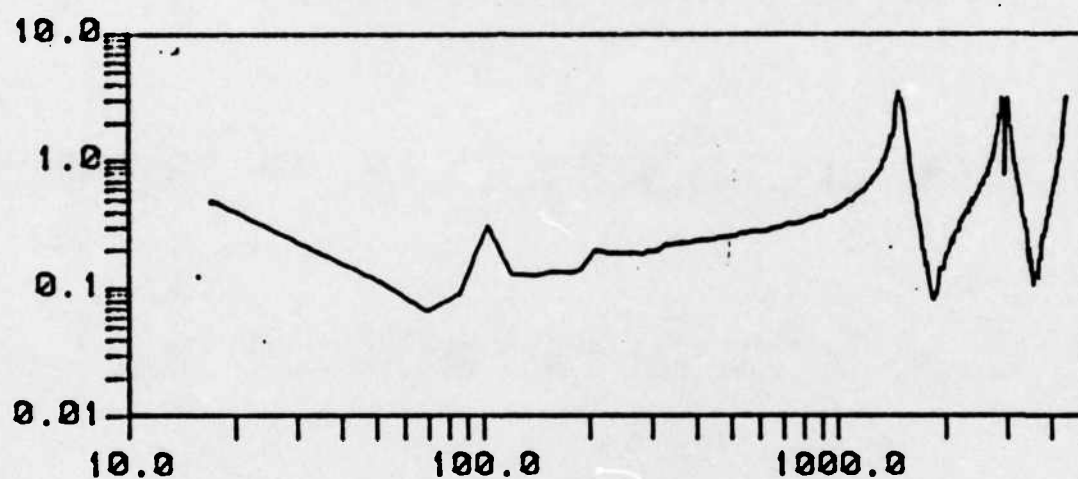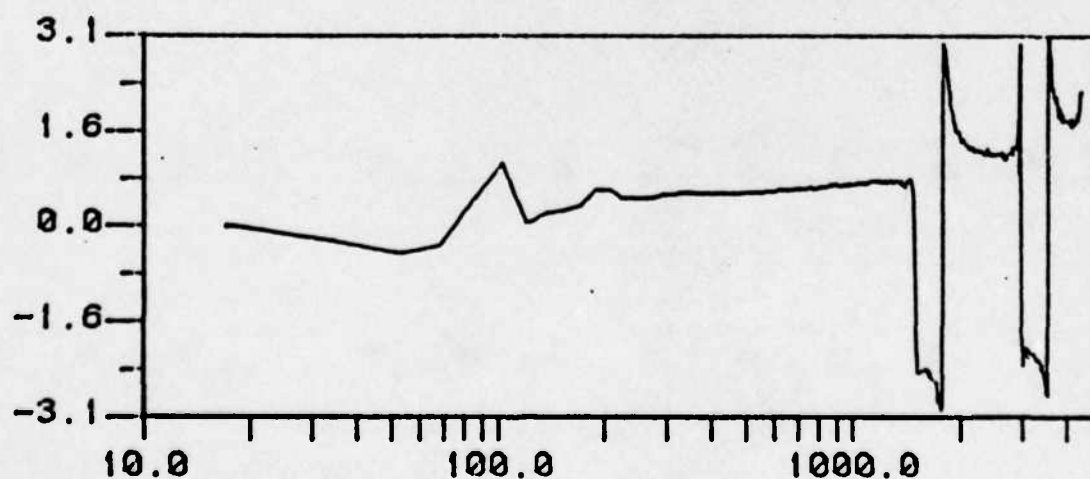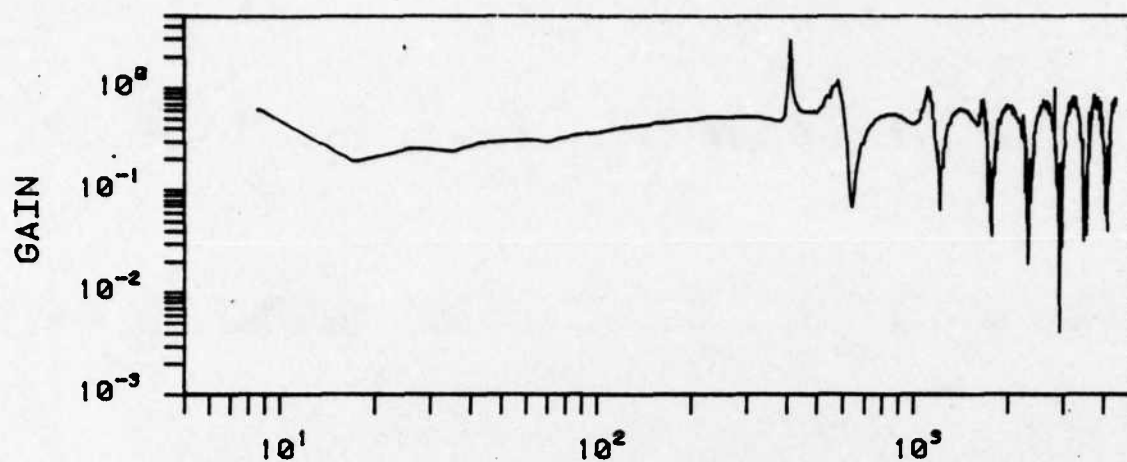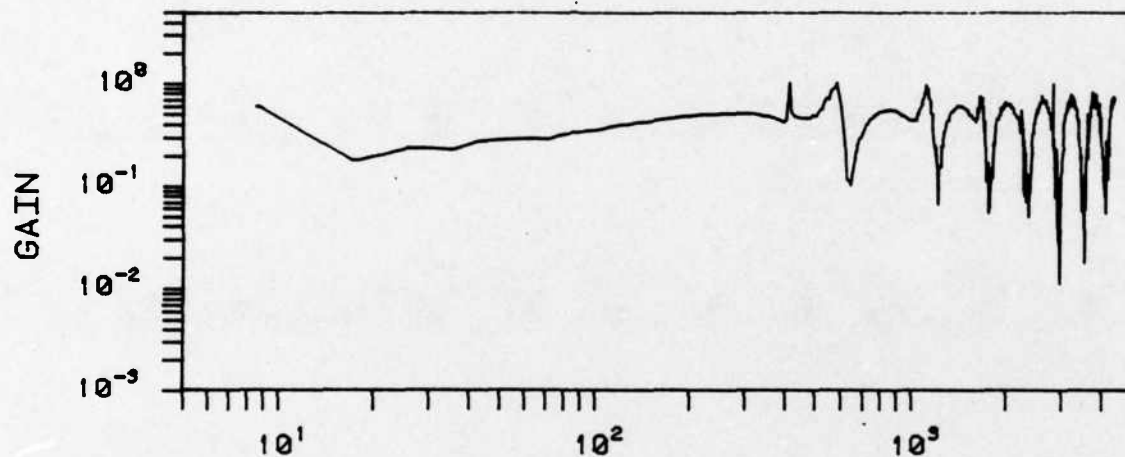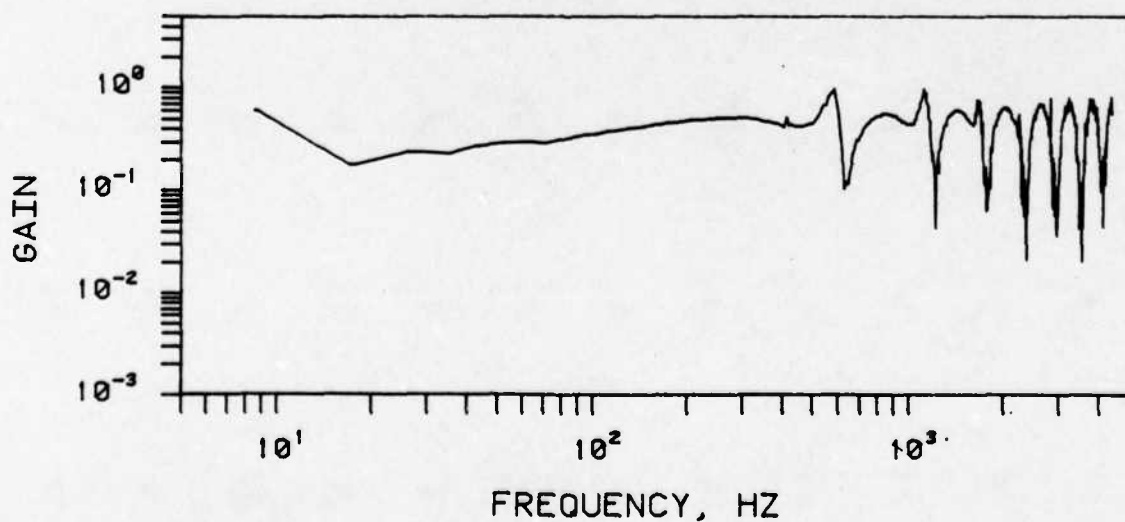The switch to new signal processing techniques halved our effective sampling rate, since both the current and the voltage are sampled. This means that we need to sample at twice the rate of before. Therefore, an A/D converter was purchased and installed which is capable of sampling at 90,000 points/second, as compared to 18,000 points/second on our previous converter. This allows us to examine the frequency response of the arc up to 22.5 kHz. Installation of this new equipment has required development of new software. However, this has been completed during the current contract period and measurements at these higher frequencies are underway.

Although the frequency response function for a linear system is independent of the input to the system, the input signal is of great importance, as the quality of the input signal affects our ability to measure the frequency response function. With this in mind, a series of experiments were carried out to determine the optimum current waveform for probing the arc.

In these experiments, various classes of input signal were passed through an electrical circuit with a known frequency response function. The input waveforms included a single rectangular pulse, a double pulse, and random noise. Representative plots of these signal types together with their gain functions and coherence function are shown in figures 4, 5, and 6. Note that the gain should be 0.1 for all frequencies up to 20 kHz for this system. As can be seen, the rectangular pulse yields spurious gain results, even though the signal seems to be very smooth. For this reason, the narrow rectangular pulse is not a very usable current waveform without further refinement. The double pulse is much better, although the resulting gain waveform is somewhat choppy. This choppy behavior can be modified by changing the relative widths and separation of the two pulses. A circuit is being
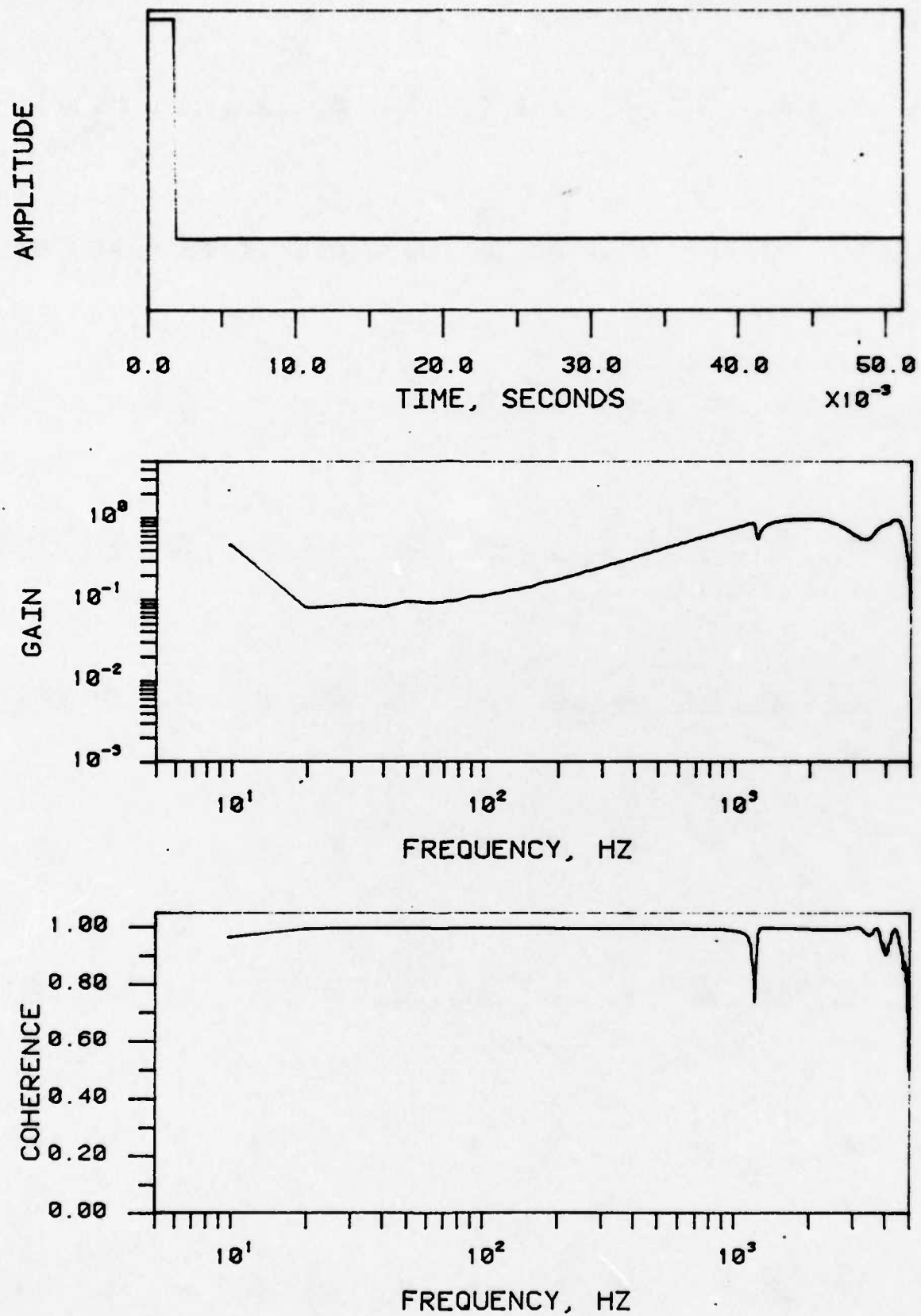
Figure 4. Time and frequency plots for rectangular pulse.
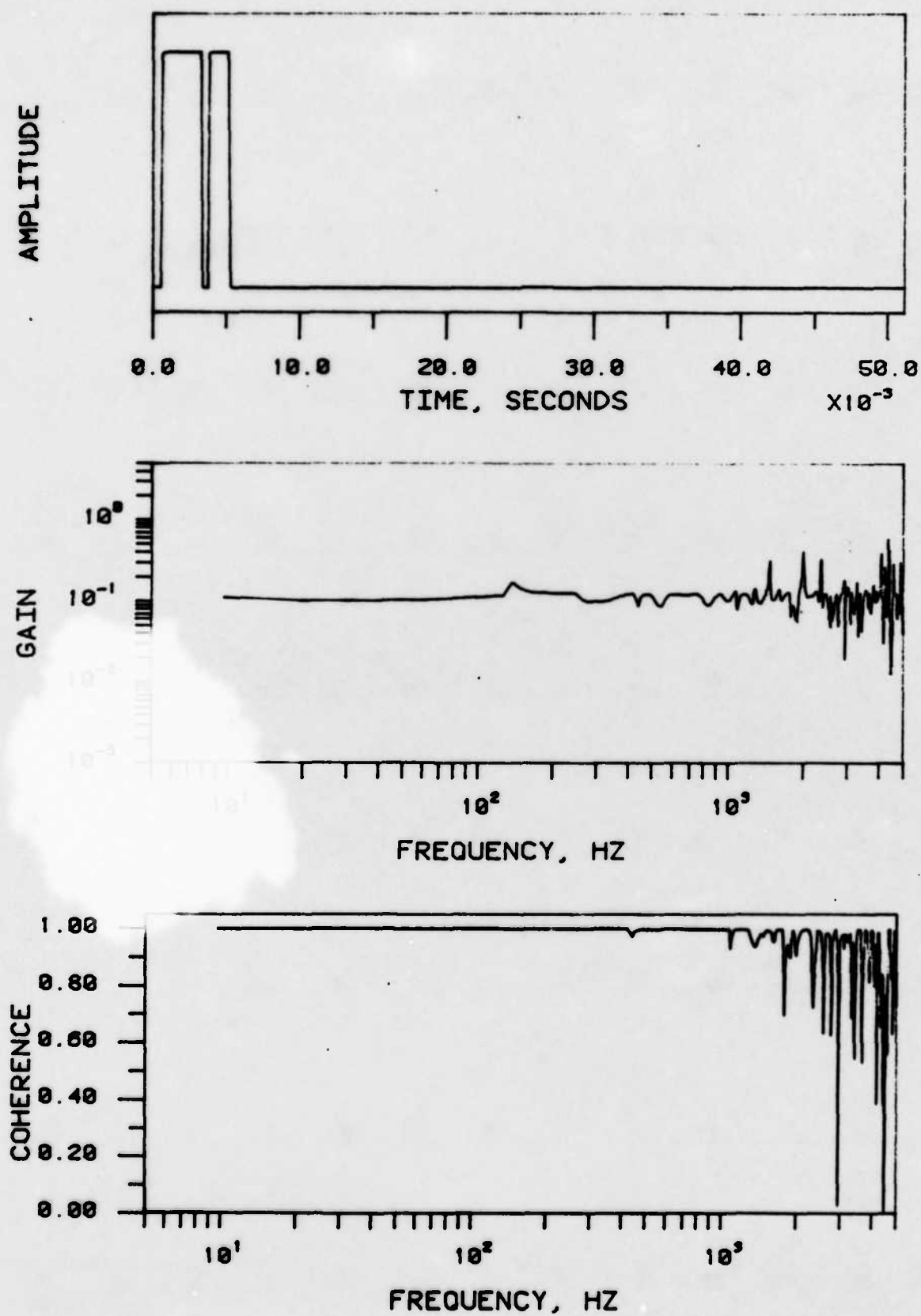
Figure 5. Time and frequency plots for double rectangular pulse.
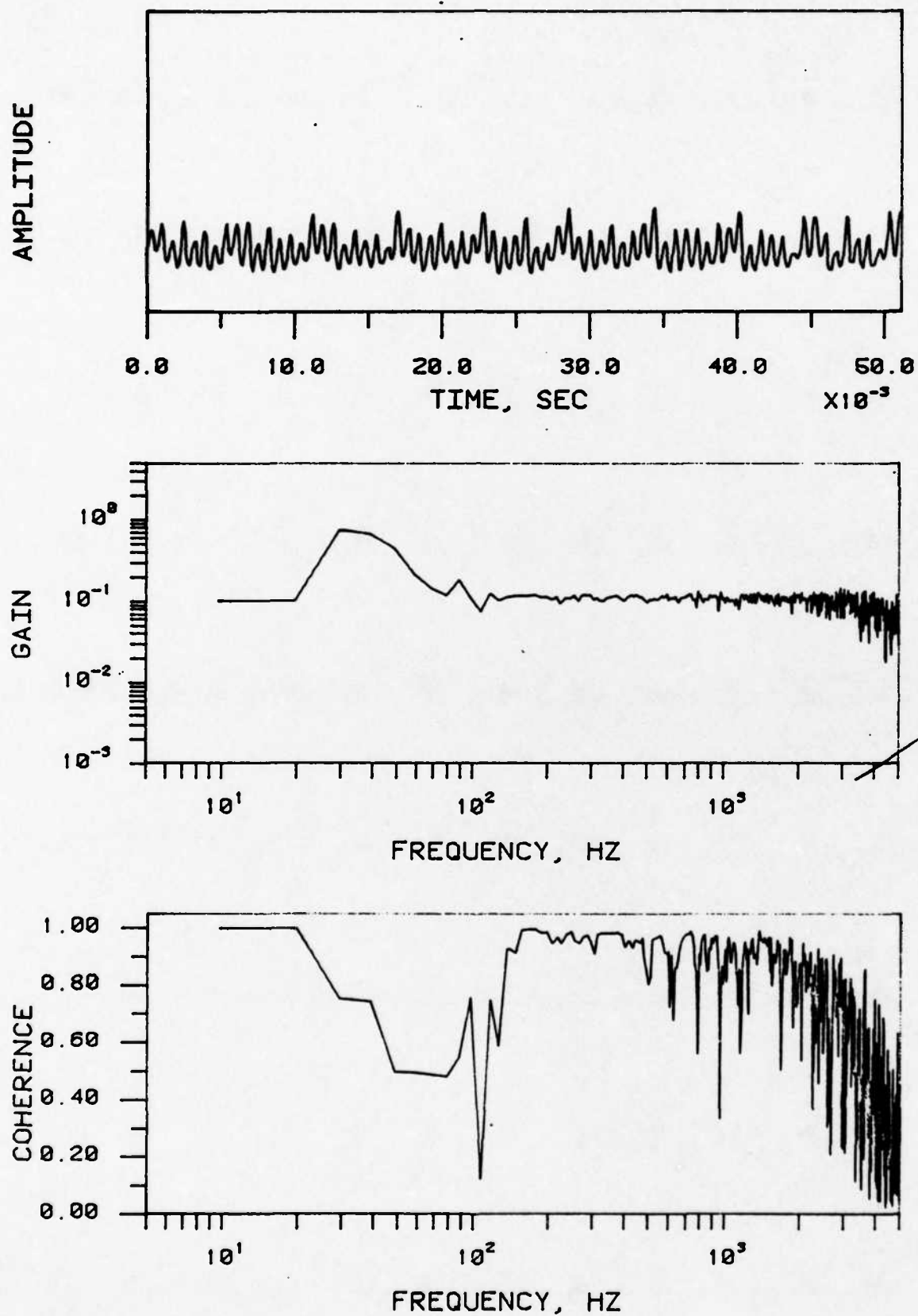
Figure 6. Time and frequency plots for random noise waveforms.

designed and tested which will allow us to make these changes. The input waveform which yields the smoothest reliable gain function is random noise. This is the form of input which is usually used for system identification. The largest drawback to the random noise waveform is the lack of availability of this type of current waveform in commercial welding power supplies.

The planned future studies on this project can be basically classified into two groups: a study of arc welding defects, and a study of puddle dynamics. In the first case, various kinds of geometric and chemical defects will be simulated in order to search for identifiable changes in the frequency response function. In the second, a concerted effort will be made to identify changes in the frequency of puddle vibrations with changes in the size of the weld puddle and the density of the liquid metal. Independent measurements of the puddle vibration frequency will be made using high-speed cinematography. In this way, a correlation will be drawn between the frequency measured by cinematography and that measured by signal processing methods.

B. Convection and Surface Depression of Arc Weld Pools

This study has produced two technical papers. The first of these, included in Appendix F, has been published and was presented at an ASME conference. The second paper, included in Appendix G, has been accepted for publication. Work is continuing in this area.

VI.   ADDITIONAL RESEARCH TOPICS

One additional paper has been prepared based upon studies conducted jointly under this contract and a contract for the U. S. Department of Energy. This is included in Appendix H. The study reported in this paper has been completed.

SUMMARY

During the past year, significant progress has been made in all areas of this project. The research conducted over this time involved spectrographic studies of the weld pool, welding of heavy section titanium, fracture toughness of HY-80 weld metal, and sensors for automation of arc welding.

REFERENCES

1. A. Block-Bolten and T. W. Eagar, "Selective Evaporation of Metals From Weld Pools", Trends in Welding Research in the United States, S. A. David, ed., ASM, Metals Park, OH, 1982, pp. 53-71.

2. T. W. Eagar, et al., "Fusion Welding Research", Third Annual Technical Report, Contract N0014-80-C-0384, April 30, 1983.

3. R. W. Richardson and R. L. Renwick, "Experimental Investigation of GTA Weld Pool Oscillations", Welding Journal, 62 (2), February 1983, p. 29s.

4. J. S. Bendat and A. G. Pierson, Engineering Applications of Correlation And Spectral Analysis, New York, John Wiley and Son, 1980.

APPENDIX A

(Accepted by "Metallurgical Transactions B")

Metal Vaporization From Weld Pools

by

A. Block-Bolten and T. W. Eagar
Materials Processing Center
Massachusetts Institute of Technology

ABSTRACT

Experimental studies of alloy vaporization from aluminum and stainless steel weld pools have been made in order to test a vaporization model based on thermodynamic data and the kinetic theory of gases. It is shown that the model can correctly predict the dominant metal vapors that form but that the absolute rate of vaporization is not known due to insufficient knowledge of the surface temperature distribution and subsequent condensation of the vapor in the cooler regions of the metal. Values of the net evaporation rates for different alloys have been measured and are found to vary by two orders of magnitude. Estimated maximum weld pool temperatures based upon the model are in good agreement with previous experimental measurements of electron beam welds.

I.   INTRODUCTION

Loss of alloying elements from the weld pool due to vaporization is important for a number of reasons. Firstly, if the loss is great enough, the mechanical properties of the weld may be impaired [1]. Secondly, the composition of a welding arc plasma influences the temperature of the arc [2], arc stability, and fume formation [3]. Thirdly, it has been shown that vaporization places an upper limit on the temperature produced on the surface of the metal due to evaporative cooling [4,5].

A previous paper has presented a formalism for calculation of partial pressures of metal vapors above steel weld pools [5]. This analysis provided an estimate of the power lost by evaporation as well as an upper bound on the surface temperature of steel weld pools as a function of alloy composition. In the present paper, this analysis is extended to evaporation from aluminum and copper alloy weld pools where different metal vapors dominate. The results of the calculations are then compared with experimental results from both aluminum and steel weld metals.

II.   EXPERIMENTAL PROCEDURE

Both steel samples and aluminum alloy samples were subjected to extended time welding in a specially adapted chamber which was coupled to a direct reading emission spectrometer. The chamber was supplied with a lens guiding the light to the spectrometer grating. A mirror imaging device was provided to ensure uniform position of the work and the electrode. The hearth was water cooled and the entire system was purged with argon flow. The rotating water-cooled copper-hearth shown in Figure 1 was employed in the case of 12.5 cm diameter 304 steel samples but the rotation has not proven useful.

The slight deviations of the rotating sample cause periodic sinusoidal changes in the arc length and corresponding oscillations in the spectral signal. Therefore, this experiment could only be characterized by lower and upper limits of spectrographic signal, voltage, current, and final weld chemical composition; and not by a uniquely defined value of each of those parameters. As a result, the experimental data presented in this paper were obtained from stationary arc welds where the arc length was more controllable.

The 0.35 to 1.10 g steel samples consisted of 1.6 mm diameter wires (502, 505, 5151 and 5212 steels) or 1.1 mm wire (410 steel) or 2.4 mm diameter wires (308L and 309L steels). The thoriated tungsten electrodes of 1.6 mm diameter were mounted as shown in Figure 1. Each steel sample was weighed before and after each experiment, yet only the 308L and 309L stainless steel samples gave resonable weight loss results (Fig. 2), as other steels were too readily oxidized in spite of the welding grade argon environment. The small amount of impurities in this gas stream and the extended time of these tests created a significant weight loss or gain by oxidation over the course of the experiment in these other steels. The compositions of the steel and Al-alloy samples used are given in Table I. The sizes of the Al-alloy samples are specified in the caption of Figure 8.

Atomic absorption chemical analysis was performed on buttons from the melted steel wires and on shavings drilled out of craters of the Al-alloy samples after melting.

The spectrographic signals were ratioed relative to the most abundant element of the alloy: Fe in steels and Al in Al-alloys, through a system of analog dividers. The spectrographic signals from the photomultipliers were

measured by Keithley Model 480 picoamperometers.

III. **PREDICTION OF VAPORIZATION TENDENCY**

As shown in a previous paper [5], the logarithm of the partial pressure of an alloy component in the gas phase is proportional to the sum of the logarithms of the standard pressure of the pure element and the activity of the element in the alloy, i.e.,

$$\log \bar{p}_A = \log p^o_A + \log a_A$$

where

$\bar{p}_A$ is the partial pressure of element A in the gas phase

p^o_A is the standard pressure of pure A, and

a_A is the activity of A in the alloy.

The vaporization rate can be predicted from the kinetic theory of gases [6],

$$r_A = 44.331 \ \bar{p}_A (\frac{M_A}{T})^{1/2} [g \cdot s^{-1} \cdot cm^{-2}] \tag{2}$$

where

r_A is the rate of evaporation of element A,

M_A is the molecular weight of A

T is the absolute temperature, and

$\bar{p}_A$ has units of atmospheres.

The evaporation power loss P_L is then

$$P_L = r_A (L_A - \overline{\Delta H_A}) [watt \cdot cm^{-2}]$$

where

L_A is the heat of evaporation of pure A and

$\overline{\Delta H_A}$ is the partial molar heat of mixing of A in the alloy.

The evaporative energy loss, E_L, is

$$E_L = r_A(L_A - \overline{\Delta H_A})t \, [\text{watt cm}^{-2} \, \text{s}],$$

where, t, is time.

In most cases $\overline{\Delta H_A}$ is small compared to the heat of evaporation. If the element of interest is the solvent such as iron in steel or aluminum in aluminum alloys, $\overline{\Delta H_A}$ can be neglected.

Using equation (1), it is possible to construct pressure–temperature diagrams for aluminum, copper and iron base alloys as shown in Figures 3, 4 and 5. These diagrams are based on tabulated values of activity coefficients (12). To extrapolate Hultgren's activity (a_o) data to other (a_n) temperatures, $\log a_n = \log a_o + \frac{\Delta G^x}{4.575}(\frac{To-Tn}{ToTn})$, $\overline{\Delta G^{xs}}$ was assumed identical to ΔH, and $\overline{\Delta G^{xs}}$ or $\overline{\Delta H}$ was used when available. $\overline{\Delta G^{xs}}$ is partial free energy of mixing.

As shown previously, mild interaction effects between the alloying elements in ternary and higher order systems can often be neglected [5], however, strong interactions where compounds tend to form in the liquid metal cannot be neglected.

As shown previously for steels [5], equation (4) can be combined with the arc surface energy distributions of Nestor [7] to produce upper limits on the surface temperature of the weld pool. Figure 6 shows such an upper bound

analysis for a number of aluminum alloys. The upper bound analysis assumes that all of the power input to the weld pool is lost by vaporization of the metal. Since this is clearly not true, a least upper bound on the temperature of the weld pool surface can be obtained if one knows what fraction of the total input power is lost by evaporation. As will be shown later, it is difficult to measure this quantity with precision. The concept of the upper bound temperature of the pool is outlined in a previous paper ((5).

IV. CORRELATION OF THEORY WITH EXPERIMENT

As noted in the experimental procedure section, a number of steel and aluminum alloys were arc melted for unusually long times in order to evaporate enough alloying components to be detectable by chemical analysis. Due to problems of oxidation, only two of the stainless steel samples gave consistent results. The Mn and Fe spectrographic signals normalized to the relatively stable Cr signals as a function of arc melting time are shown in Figure 7. It will be noted that Mn is the primary element lost as predicted by Figure 5.

In order to test the model more completely, a series of six aluminum alloys with varying zinc and magnesium contents were selected. Aluminum alloys were selected because the Zn and Mg have very high vapor pressures as compared to aluminum; and as seen in Figure 6, this significantly lowers the upper bound temperature.

The aluminum alloys can be separated into four groups, where

I   Zn vapor dominates,

II   Mg vapor dominates,

III   Nearly equivalent Zn and Mg vapor pressure exists,

IV   Al vapor dominates.

Alloy 7075 belongs in group I as seen in Figure 8. If we compare Table II and Figure 3, we see that the high zinc concentration in 7075 alloy places the zinc isopleth of Figure 2 well above the Mg isopleth for this alloy.

Alloys 5083 and 5456 belong to group II as seen in Figure 9 and 10. This is again consistent with the predictions made from Table II and Figure 3.

Alloys 6061 and 2024 belong to group III as shown in Figures 11 and 12 respectively. This result is not as easily predicted from Figure 3 since the exact composition of the alloy and the temperature of the weld pool surface are not known precisely. Nonetheless, the spectrographic data of Figure 13 clearly show a simultaneous rise in the spectral signals for both Mg and Zn. It is interesting to note that Zn typically reaches its maximum presence in the vapor later than Mg; probably due to kinetic limitations since Zn is more dilute in the alloy. The gradual rise of both elements is most likely due to increase in the size of the weld pool with time. Alloy 1100 is the only sample tested which belongs to group IV of the series.

Summarizing, Figures 8 to 12 show the analyses taken from the weld pools of different Al-Alloys during extended time welding. The 7075 Alloy with Zn-vapor domination (Figure 8) exhibits changes only in Zn content, while Mg content stays constant. In Figures 9 and 10, the Mg-vapor dominated 5083 and 5456 alloys show Mg-content falling off, while Zn-content stays constant, or below the detection level. Figures 11 and 12 for alloys 6061 and 2024 prove that both these alloys exhibit mixed vapor domination and both Zn and Mg contents change with time. In addition, SEM semiquantitative analyses have

also shown changes in Zn only for the 7075 alloy, changes in Mg only for 5083 and 5456 alloy, and changes both in Mg and Zn content for the 2024 and 6061 alloys.

From Figures 8, 9, 10, 11 and 12, values of apparent initial evaporation rate, apparent long term (mean) evaporation rate, and apparent evaporation per unit of energy have been calculated. The latter value is normalized to gross energy input [8,9] which is half of the total arc power input, as the other half is lost to the environment and does not enter the weld pool. All these values, together with percentages (referred to theoretical evaporation per unit energy $(L - \overline{\Delta H})^{-1} [J^{-1}])$ are displayed in Table III. It is seen that the net power lost by vaporization is much less than one percent of the total power input to the metal. As will be discussed later, this is much less than the abolute evaporative power loss, however, much of the absolute evaporative power is regained by condensation of the vapors in cooler regions of the weld pool.

IV.. DISCUSSION

The preceeding results indicate that the model can effectively use existing thermodynamic data to predict the dominant metal vapors above the weld pool; however, it would be useful if one could predict weld pool surface temperature and hence the rate of alloy element loss. This proves to be a much more difficult task.

Quigley, et al. [9] have estimated the evaporative power loss from a gas tungsten arc to be of the order of 2 percent of the total power. If this is true, it would reduce the upper bound temperatures based on 100 percent evaporative power loss as shown in Figure 6 and in Table II. Indeed if one

were to assume absolute evaporative power loss to lie between 1 and 10 percent of the total power, the surface temperature limit would drop by 200 to 500°C for aluminum alloys. Table II shows that the surface temperature of aluminum alloy arc welds could vary from just above the melting temperature to 700°C superheat depending on alloy composition and the amount of heat lost by vaporization.

As shown in Table III and Figures 8 through 12, weight loss measurements based on alloying element loss from the weld samples gives net evaporative losses between zero and $95 [\mu g \cdot s^1 \cdot cm^2]$. This corresponds to maximum net vaporization losses of roughly 0.015 percent of the net incident power; however, it is believed that more metal than this is vaporized from the center of the pool and then recondenses on cooler regions, thus recycling through the system. This is indirectly confirmed by spectrographic monitoring of calcium vapor in 304 stainless steels [10]. The calcium spectrographic lines remain strong and do not diminish after 15 minutes of welding even though there is only 10 ppm Ca in the steel. The only way this small amount of Ca could remain after such a long time is if it is "recycled" into the metal by condensation. Although it is not possible to measure how much vapor condenses back into the pool rather than is lost, it is believed that a larger fraction of Zn recondenses back to the pool than is lost from the system. In a sense, this is confirmed by the temperatures calculated for the 7075 alloy in Table II. If the temperature were low enough for only 0.015 percent of the power to be lost by vaporization, then the liquid would be cool enough to solidify. It is clear that at least several percent of the power at the center of the 7075 alloy pool must be lost by zinc vaporization. Much of this power is recovered at the edges of the pool as the vapor

condenses. Because of this evaporation-condensation process it is very difficult to determine the absolute vaporization rate with any accuracy.

Schauer et al. used an infrared pyrometer to measure the weld pool surface temperature of electron beam welds in steel and aluminum [11]. If one assumes that the power lost from the electron beam weld pool is 6000 watts $\cdot cm^{-2}$, the measured temperatures are in reasonable agreement with the values predicted by the model presented here as seen in Table IV. Indeed, these results are perhaps the most conclusive in showing that evaporative power losses set an upper limit on the surface temperature of a weld pool. In general, these power losses probably lie between 1 and 10 percent of the total power, but the value varies somewhat with alloy content and with input power density. These losses provide a prediction of maximum arc weld pool surface temperatures between the melting point and 1600°C for aluminum alloys and between 2000°C and 2500°C for steels. The high energy density processes such as laser and electron beam can produce even higher surface temperatures with greater rates of alloy vaporization than arc welds.

V. CONCLUSIONS

A thermodynamic model of vaporization from weld pools has been presented which can predict the dominant metal vapors that form during welding in the absence of strong compound forming elements such as oxygen or nitrogen. The evaporative power loss in arc welding lies between 1 and 10 percent of the incident power, although more precise measurement is difficult due to condensation of metal vapors in cooler regions of the weld pool. These vaporization rates place upper limits on the surface temperature of the weld pool. These limits are in good agreement with measurements on different

alloys when using electron beam welding, but the results for arc welding are somewhat lower than the temperatures often assumed for arc weld pools. It is concluded that the metal vaporization from the weld pool places a limit on the maximum temperature of the pool which is significantly less than the boiling temperature of the metal. The presence of volatile alloying elements may further reduce this maximum temperature limit.

Table IV indicates that apparent evaporation rates (initial and mean) confirm Zn domination in the group I alloys, Mg domination in group II, and co-domination of Zn and Mg in group III alloys.

The largest absolute evaporation seen occurs in the Zn dominated group I followed by Mg dominated group II. The apparent percentages of the total energy are very small indicating that the vapors are subjected to multiple recycling during extended time arc welding.

VI. ACKNOWLEDGEMENTS

REFERENCES

1. D. W. Moon and E. A. Metzbower, *Welding Journal*, 1983, Vol. 62, pp. 53s-58s.

2. S. S. Glickstein, *Welding Journal*, 1976, Vol. 55, pp. 222s-229s.

3. R. F. Heile and D. C. Hill, *Welding Journal*, 1975, Vol. 54, pp. 201s-210s.

4. J. D. Cobine and E. E. Burger, *J. Appl. Phys.* 1955, Vol. 26, pp. 895-900.

5. A. Block-Bolten and T. W. Esgar, *Trends in Welding Research in the United States*, S. A. David, ed., ASM, Metals Park, OH, 1982, pp. 53-73.

6. S. Dushman, J. M. Laferty, ed., 2nd Edition, *Scientific Foundations of Vacuum Technique*, John Wiley, New York, 1962, pp. 691-737 and pp. 15-21.

7. O. H. Nestor, *J. Appl. Phys.*, 1962 Vol. 33, pp. 1638-1648.

8. N. Christensen, V. Davies and K. Gjermundsen, *British Welding J.*, 1965, Vol. 12, pp. 54-75.

9. M. B. C. Quigley, P. H. Richards, D. T. Swift-Hook and A. E. F. Gick, *J.*

Phys., D-Appl. Phys., 1973, Vol. 6, pp. 2250-2258.

10.   G. Dunn, M.I.T., Cambridge, MA, Unpublished research, 1982.

11.   D. A. Shauer,   W. H. Giedt, S. M. Shintaku, Welding Journal, 1978, Vol. 57 pp. 127s-133s.

12.   R. Hultgren, P. D. Desai, D. T. Hawkins, M. Gleiser, and K. K. Kelley, Selected Properties of Binary Alloys, ASM, Metals Park, Ohio, 1973.

FIGURE CAPTIONS

Fig. 1 Water-cooled turntable and gas-cooled electrode-holder.

Fig. 2 Weight-loss experiment. 1 - weight loss curve for 308L stainless steel, 2 - for 309L stainless steel; average voltage 11V, current set at 15A; average sample size 1g.

Fig. 3 Aluminum Alloys: Vapor pressures for some constituent alloy additions.

Fig. 4 Copper Alloys: Vapor pressures for some constituent alloy additions.

Fig. 5 Steels: Vapor pressures for some constituent alloy additions. Numbers on curves represent weight percentages.

Fig. 6 Normal mode and Cathode Spot Mode temperature distributions for the 5456 Al-Alloy. The temperature is plotted vs. non-dimensional distance $r/$ from the center of the arc; is defined as in (5) as $\rho = \sqrt{V/2\pi C}$ where V is the total power of the arc in [watts] and C is the peak power density in watt $\cdot$ cm^{-2}. The plots are based on Fig. 3 and on Nestor's (7) power distribution curves. Should 100% of energy go into evaporation of pure Aluminum, point A on temperature ordinate would correspond to the expected maximum temperature of the weld pool. Points B and C mark 10% and 1% energy going into evaporation respectively. Curves 1 are normal distribution (of energy) curves

for pure aluminum. Curves 2 are those based on Nestor for pure Al. Curves 3 are for evaporation of 0.25% Zn in Al, curves 4 and 5 are for evaporation of 4.7% Mg in Al and 5.5% Mg in Al respectively.

Fig. 7 Decay of normalized signal ratios of iron to chromium and manganese to chromium (Cr content does not change significantly) for three different steels. As can be seen Mn dominates over the iron in the vapor phase. Only after long periods of time does iron start to dominate in the 5151 and 502 steels.

Fig. 8 Loss of Zn versus energy input in [KVA min] from Aluminum Alloy 7075. No change in Mg was found. Original contents of Mg and Zn were 2.3% and 5.6% respectively. The voltage during tests varied between 12.5 and 15V; current was set between 125A and 150A; the longest experiment lasted 45 min. The size of the samples was 52 x 51 x 12.7 mm. Rates of evaporation for this and other alloys are given in Table III.

Fig. 9 Aluminum Alloy 5083. Loss of Mg versus energy input. The change in Zn content occurs only in the first few seconds of the experiment, then Zn remains constant. The original Mg content was 4.3%. Voltage and current were 15V and 125A. The longest experiment lasted 45 min.

Fig. 10 Aluminum Alloy 5456. Loss of Mg versus energy input. The changes in Zn content occur only in the first seconds of the experiment; then Zn

remains constant. Original Mg content 5.8%. Average voltage was 15V, current was set between 125 and 150A The longest experiment lasted 45 min.

Fig. 11 Aluminum Alloy 6061. Loss of Mg and Zn versus energy input. Original Mg content was 0.95%, the original Zn content 0.06%. Average voltage 14 V; the current was set at 150A. Longest experiment lasted 45 min.

Fig. 12 Aluminum Alloy 2024. Loss of Mg and Zn content versus energy input. Original Mg content 1.5%, Zn content 0.06%. Average voltage was 14V, the current was set at 150A. Longest experiment lasted 30.2 min.

Fig. 13 Signal ratios of Mg and Zn normalized to Aluminum, as typically observed for the 6061 Aluminum Alloy. The Mg/Al signal ratio is magnified 10 times.

Table I

Compositions of Starting Materials Used in This Study

Steels: Compositions as delivered

Steel #	% Fe	% Mn	% Cr
410	86.70	0.45	12.03
502	94.87	0.45	4.00
505	89.70	0.45	9.06
5151	98.05	0.54	0.99/1.37
5212	97.30	0.55	1.91
308L	67.25	1.91	21.00
309L	59.65	1.79	26.08
304	68.80	1.75	18.66

Al Alloys: Compositions as Delivered

Alloy #	Zn%	Mg%
7075	5.82	2.30
5083	0.014	4.06
5456	0.019	5.20
6061	0.063	0.95
2024	0.058	1.46
1100	<0.010	<0.010

Table II

Calculated Center Line Surface Temperatures of Weld Pools for Six Aluminum Alloys

1100 Alloy, 0-0.1% Zn*; bal. Al.

Power Density %	Vapor Domination	t°C Range NM/CSM
100	Al	1935*/2091
10	Zn*, Al	1364*/1614
1	Zn*,Al	968*/1530

2024 Alloy, 0.25% Zn; 1.2-1.8%* Mg

Power Density %	Vapor Domination	t°C Range NM/CSM
100	Mg	1422*/1751
10	Mg	1101*/1290
1	Zn, Mg*CSM	870*/975

5083 Alloy, 0.25% Zn; 4-4.9%* Mg

Power Density %	Vapor Domination	t°C Range NM/CSM
100	Mg	1268*/1491
10	Mg	994*/1126
1	Mg	807*/905

5456 Alloy, 0.25% Zn; 4.7-5.5%* Mg

Power Density %	Vapor Domination	t°C Range NM/CSM
100	Mg	1220*/1451
10	Mg	964*/1104
1	Mg	783*/891

6061 Alloy, 0.25% Zn; 0.8-1.2%* Mg

Power Density %	Vapor Domination	t°C Range NM/CSM
100	Mg	1513*/1882
10	Zn, Mg*	1154*/1358
1	Zn	870*/994

7075 Alloy, 51.-6.1*Zn, 2.1-2.9% Mg

Power Density %	Vapor Domination	t°C Range NM/CSM
100	Zn	1057*/1242
10	Zn	795*/909
1	Zn	612*/695

Normal Mode NM 200 A, 14.0 V, C = 2180[watt·cm^{-2}]

Cathode Spot Mode CSM 200 A, 14.8 V, C = 6120[watt·cm^{-2}] peak power density

* Note that the lower calculated temperatures correspond to the higher alloy compositions.

Table III

Net Energy Lost From Weld Pool by Evaporation of Alloying Elements

Group	Al-Alloy	Evaporating Element	Apparent Initial Net Evaporation Rate [μgs⁻¹cm⁻²]	Apparent Long-Term (Mean) Evaporation Rate [μgs⁻¹cm⁻²]	Theoretical Evaporation Energy $(L-\Delta H)^{-1}$ [μgJ⁻¹]	Apparent Evaporation Per Gross Energy Input* [μgJ⁻¹×10³]	Percent of Arc Energy Lost by Evaporation	Source of Data (Figure #)
I	7075	Zn	94.9	30.5	631.1	91.4	0.0144	8
		Mg	-	-	173.5	-	-	
	5083	Zn	(11.3)	∿0	631.1	38.0	0.0060	9
		Mg	5.6	12.1	173.5	40.6	0.0235	
II	5456	Zn	-	∿0	631.1	-	-	10
		Mg	9.7	12.7	173.5	49.0	0.0280	
		Al**	0	(90 to 230)	92.8	-	-	
	6061	Zn	1.2	1.2	631.1	3.6	0.0006	11
		Mg	0	1.2	173.5	3.6	0.0021	
III	2024	Zn	12.0	1.3	631.1	3.8	0.0006	12
		Mg	10.0	3.4	173.5	3.4	0.0020	

* gross energy input, ref (8,9).

** from soot formation and Al-ball growth.

Table IV

Comparison of Predicted Welding Temperatures and Temperatures Measured by Schauer et al (11).

Al-Alloy, Steel or Metal	Maximum Predicted Temperatures (CSM) if 10% or 100% Energy went into Evaporation	Dominating Vapor Species at CSM if 10% | 100% went into evaporation		Schauer's (1) Electron Beam Temperatures t°C
Aluminum	1775 / 2091	Al	Al	
1100	1614 / 2091	Zn	Al	1900±100 (1990 to 2055)*
2024	1290 / 1751	Mg	Mg	1700±100
5083	1126 / 1491	Mg	Mg	1250±100
5456	1104 / 1451	Mg	Mg	
6061	1358 / 1882	Mg	Mg	1800±100 (1800 to 1890)*
7075	909 / 1242	Zn	Zn	1080±100 (1380 to 1485)*
Steels with 0.5% Mn	2190 / 2520	Mn	Fe	2290±60; HY-130 st
Steels with 2.0% Mn	2010 / 2520	Mn	Fe	2100±50; 304 st
20-6-9 Steel		Mn	Mn	1820±40
Tantalum		Ta	Ta	4400±150

(*) Data from Schauer's figures, not matching tabulated temperatures.
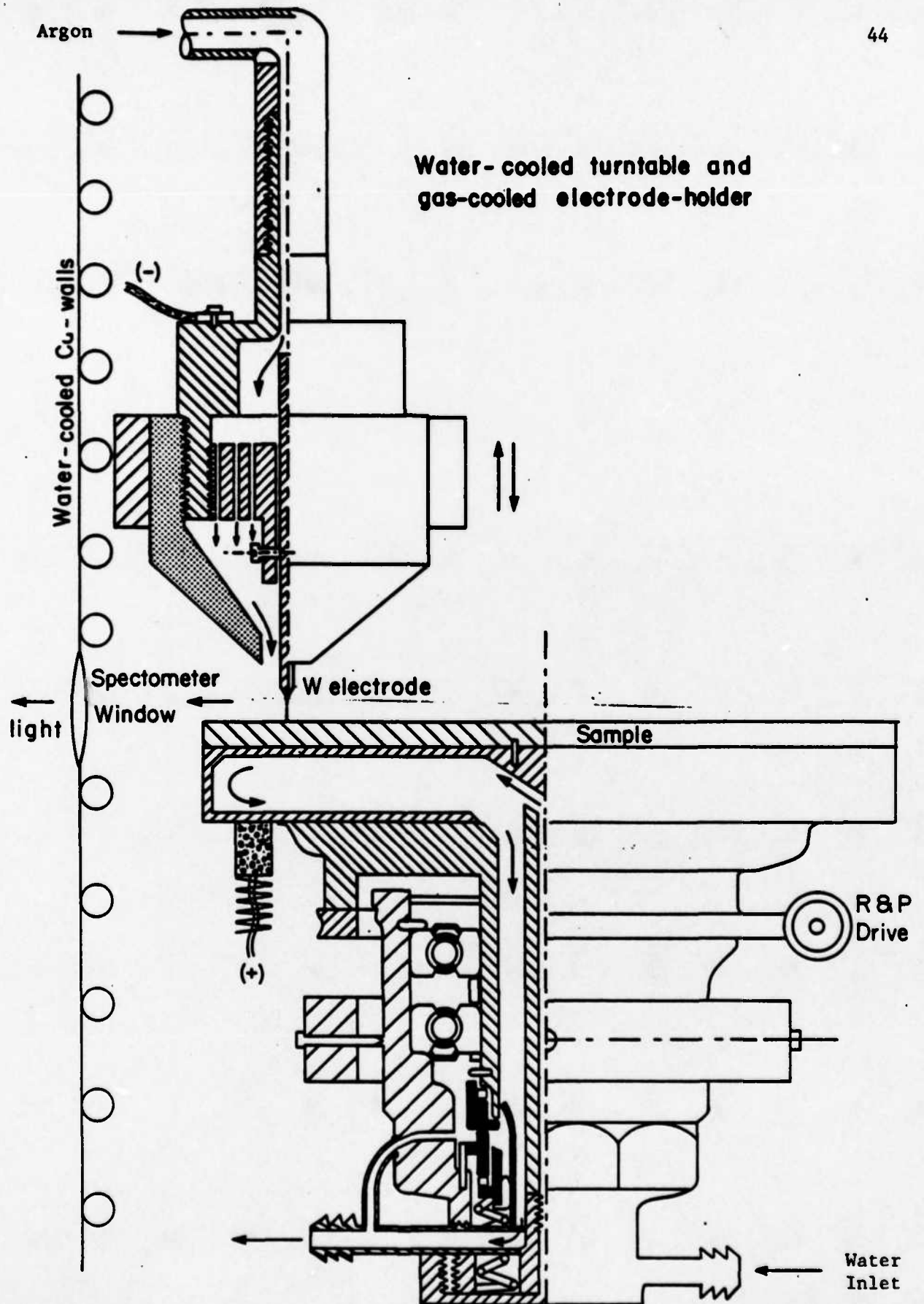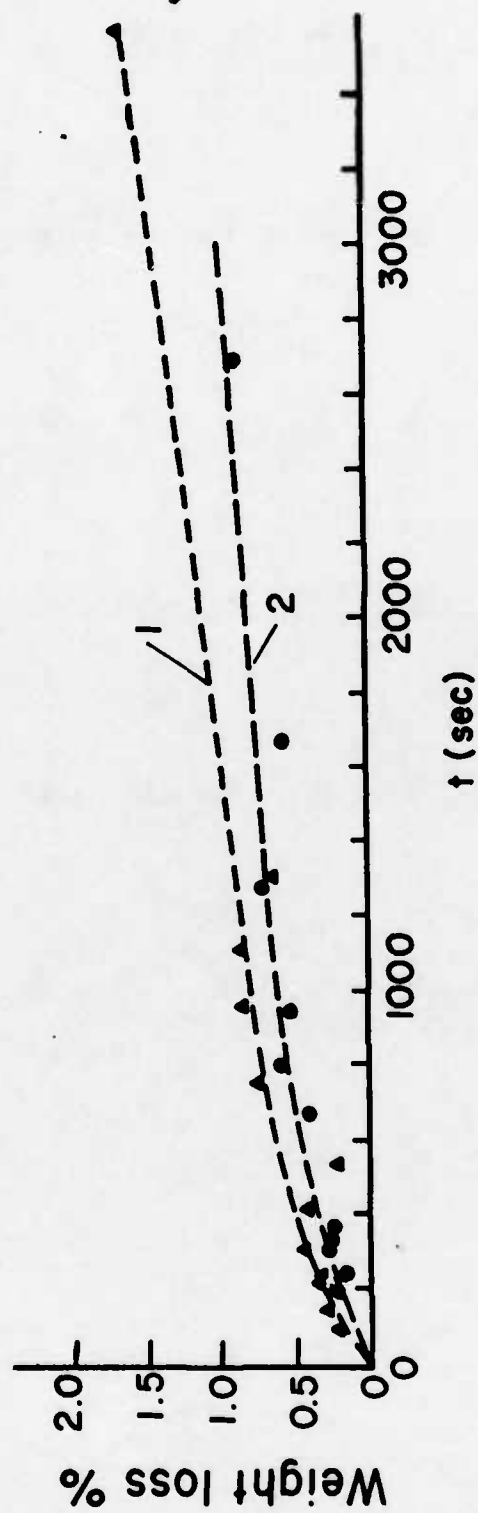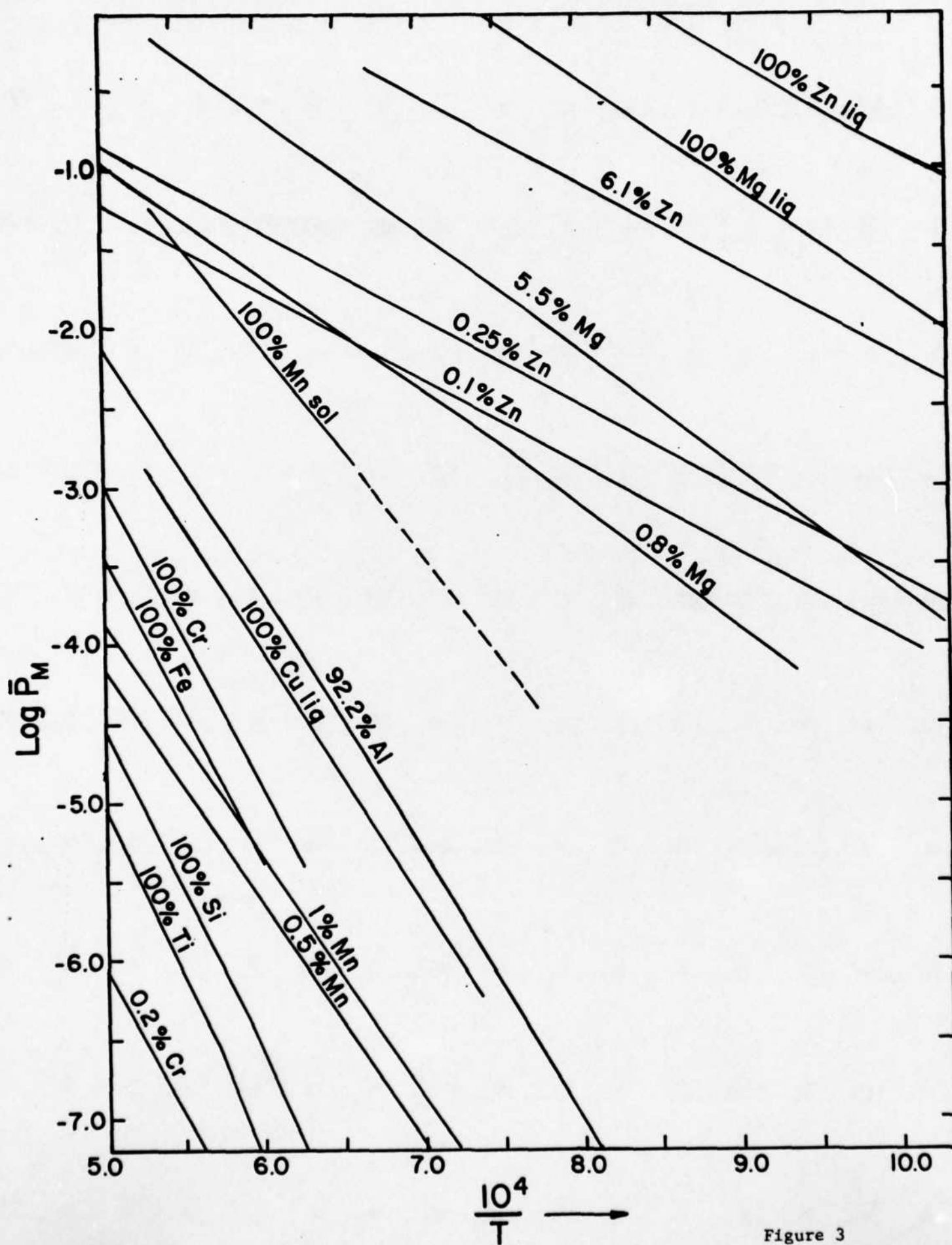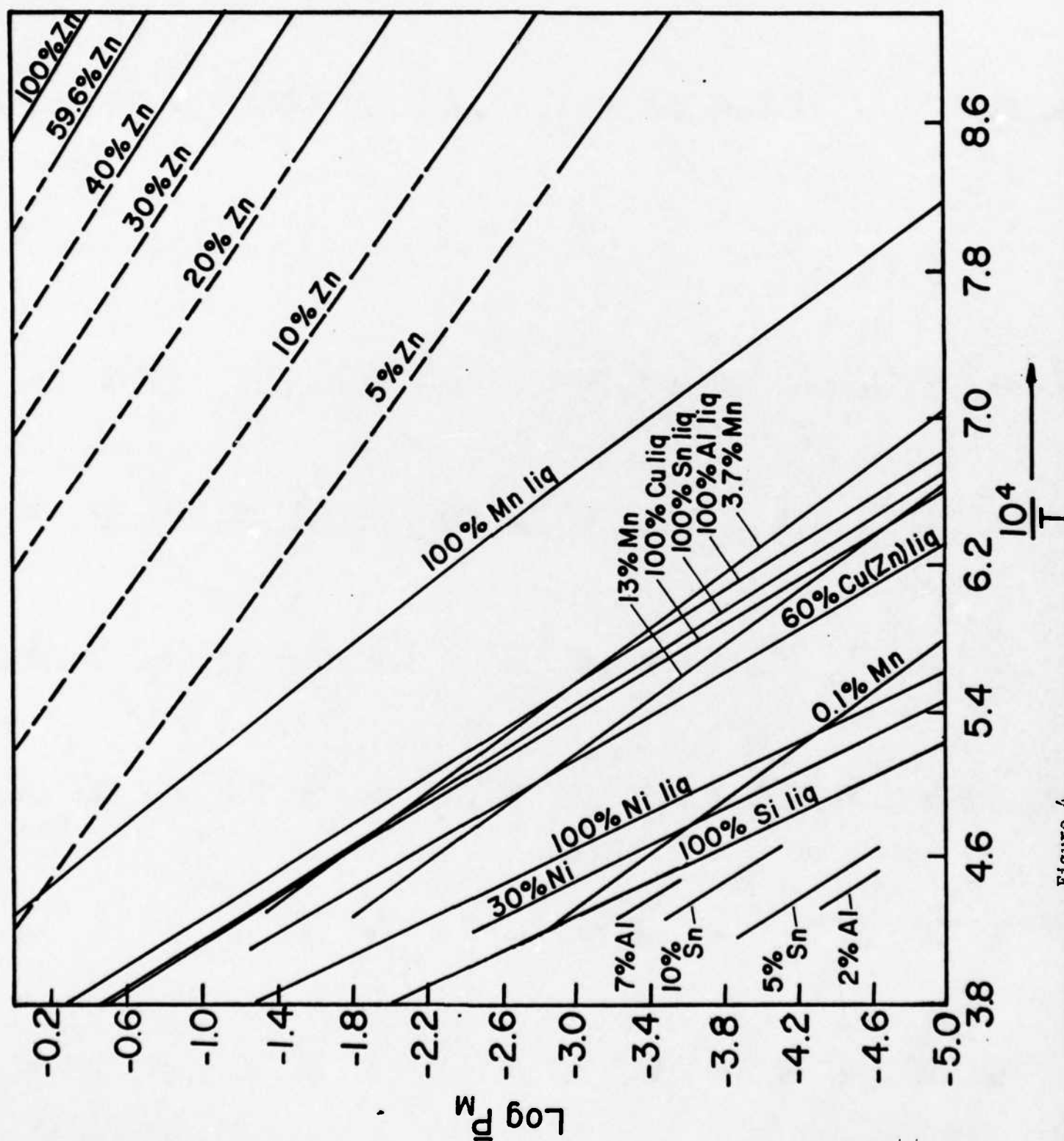
Water- cooled turntable and
gas-cooled electrode-holder

Figure 1

Figure 2

Figure 3

Figure 4

Figure 5

Figure 8

5083

Mg ——
Zn - - -

Mg %
5.0
4.0
3.0
2.0
1.0

Zn %
0.0

Mg

Zn

0   20   40   60   80   100   52

VIt [kVA min]
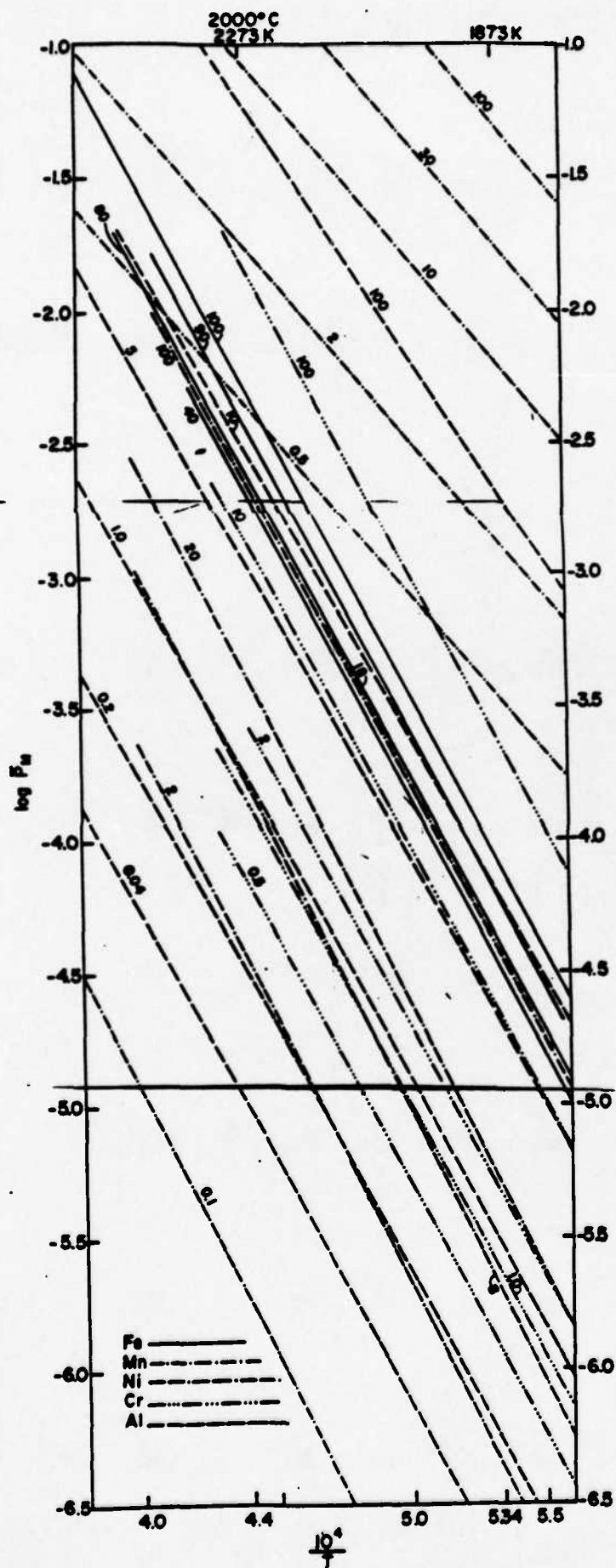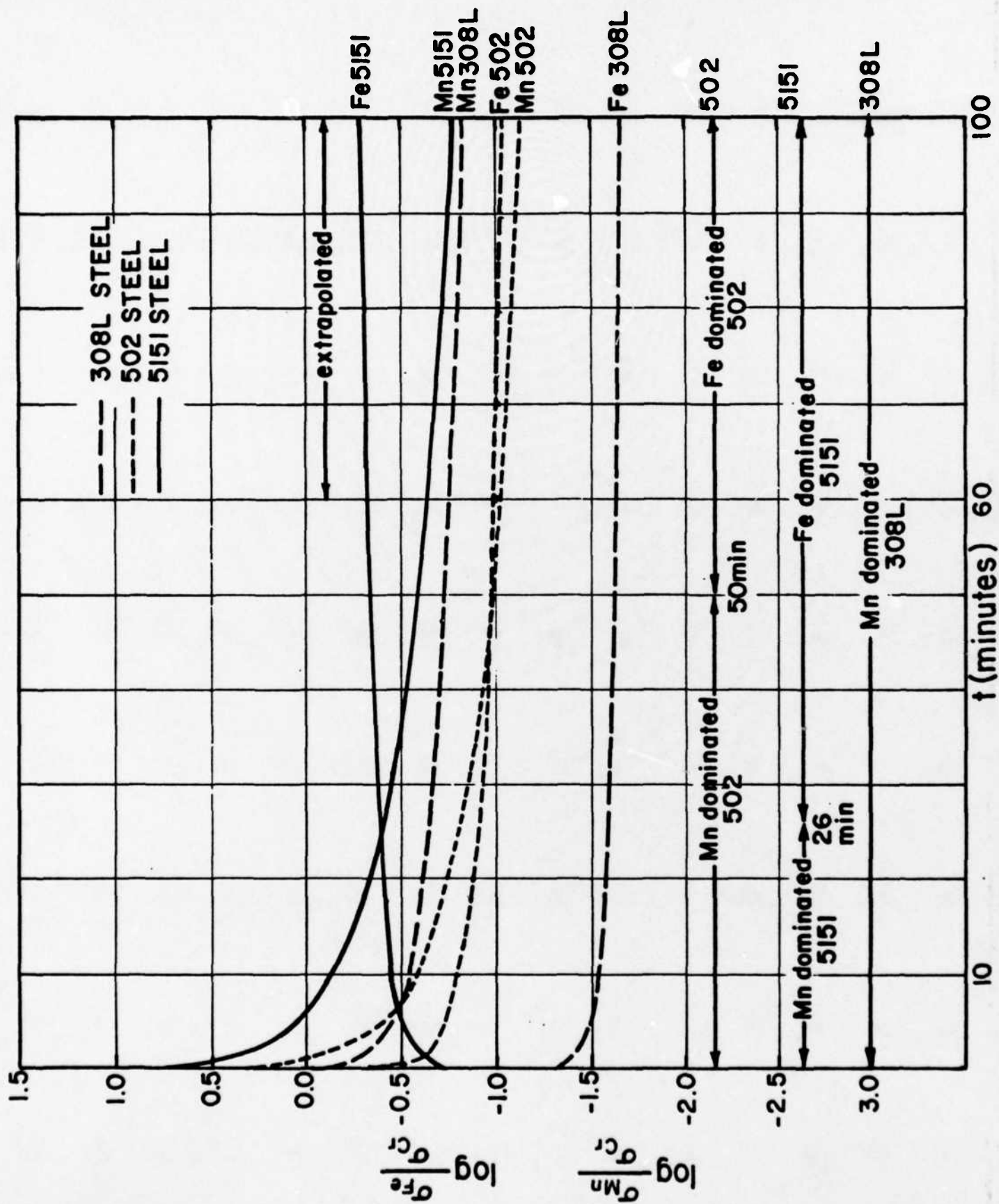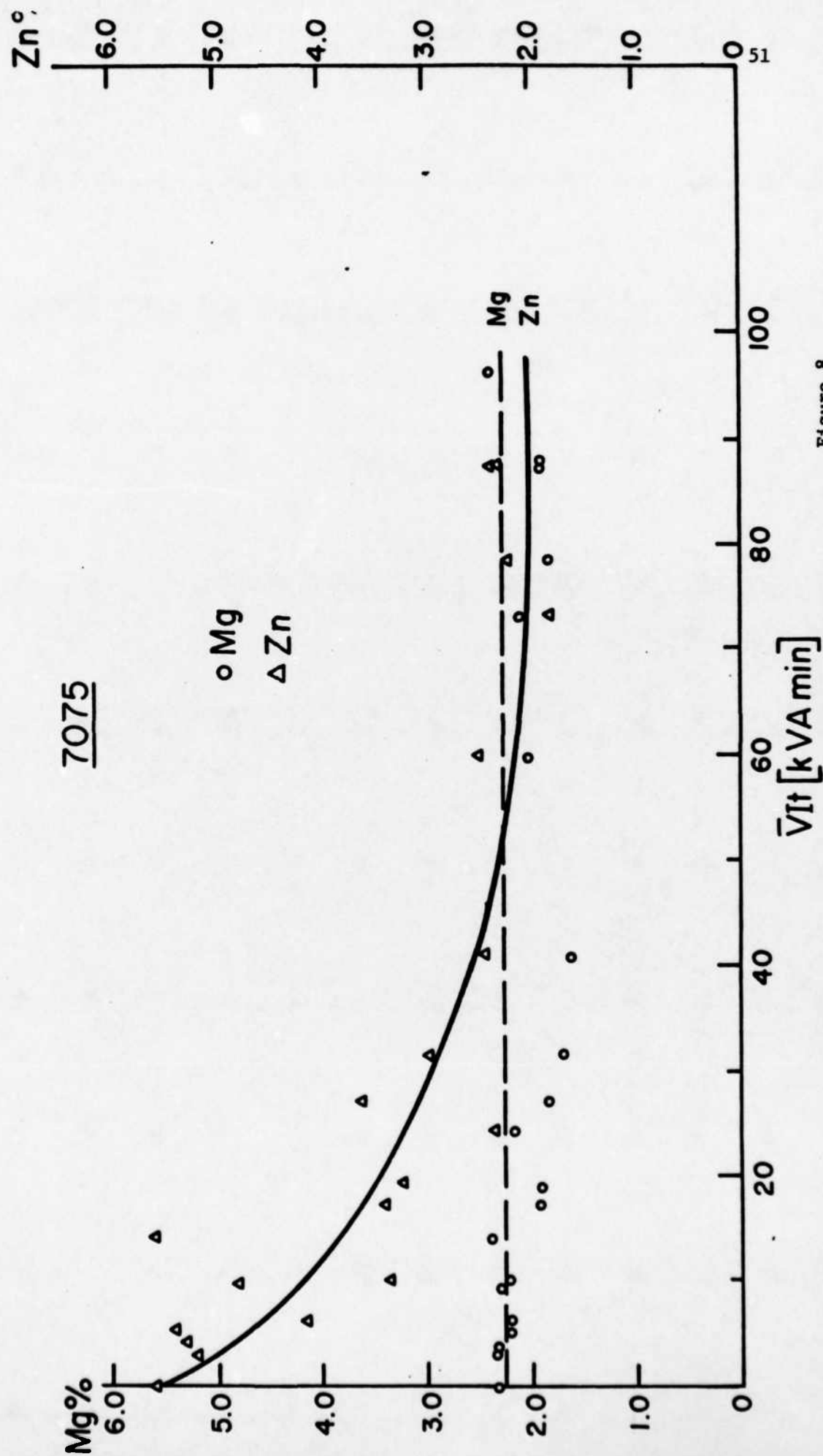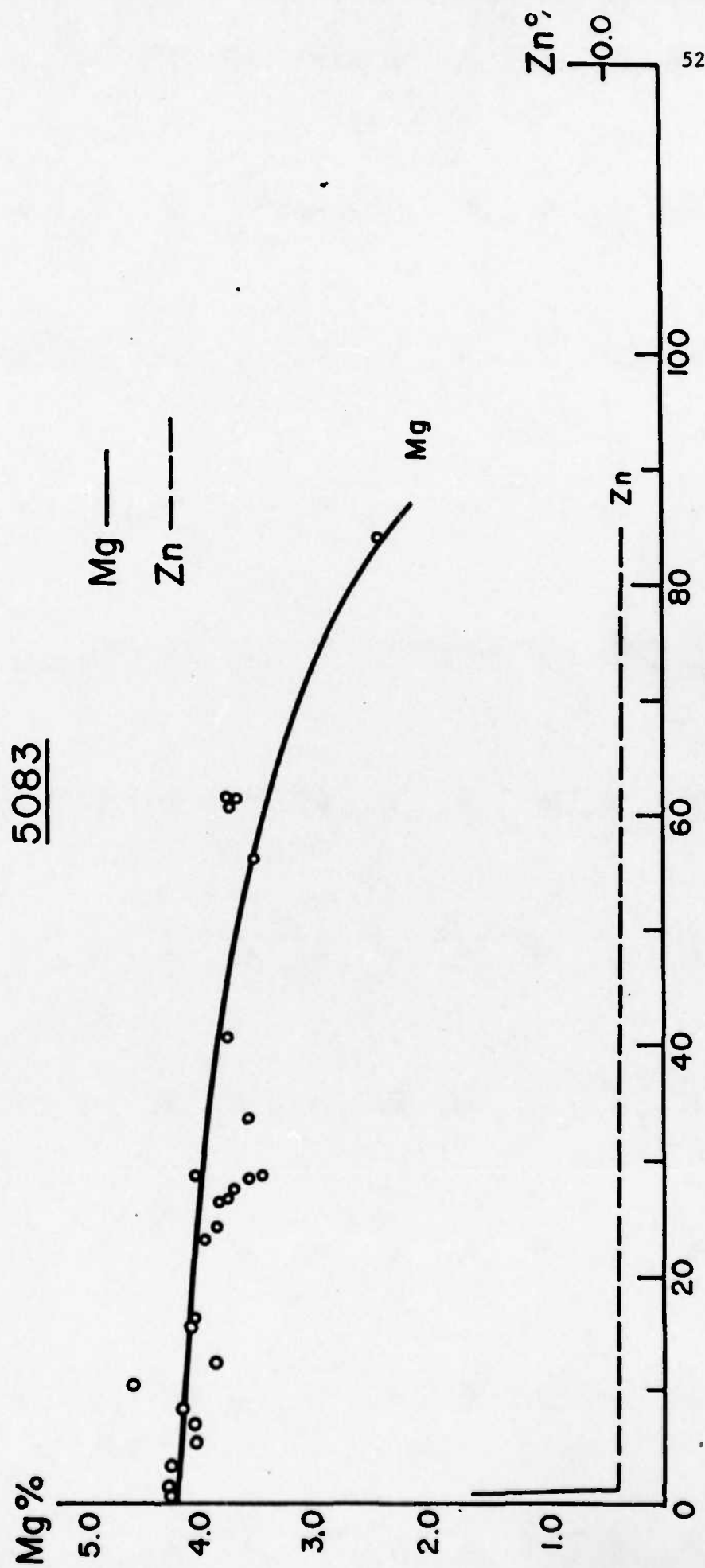
Figure 9.

Figure 10

Figure 11

54

Figure 12

6061 Al Alloy

Mg/Al

Zn/Al

t (min)

Signal ratios

Figure 13

APPENDIX B
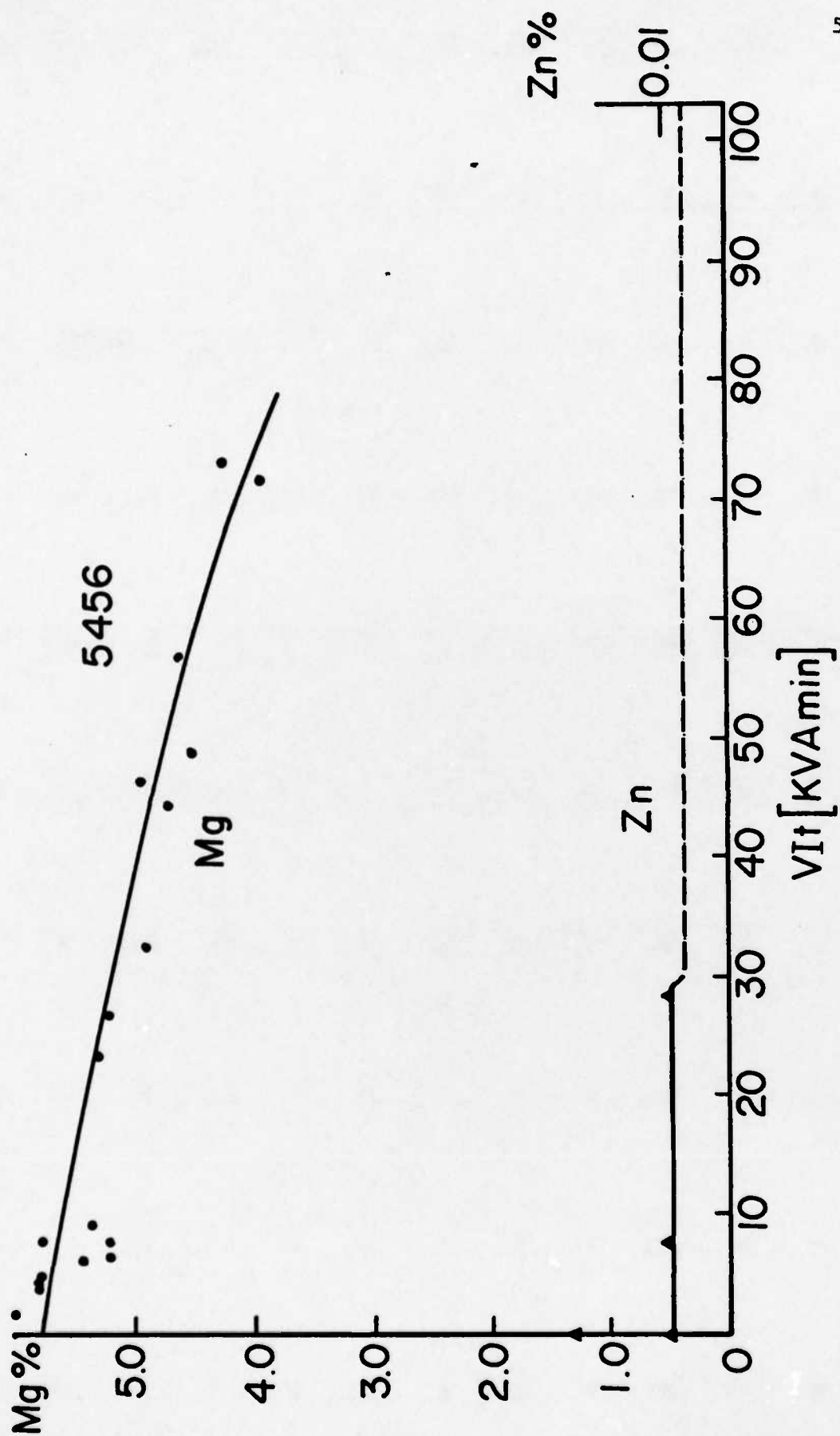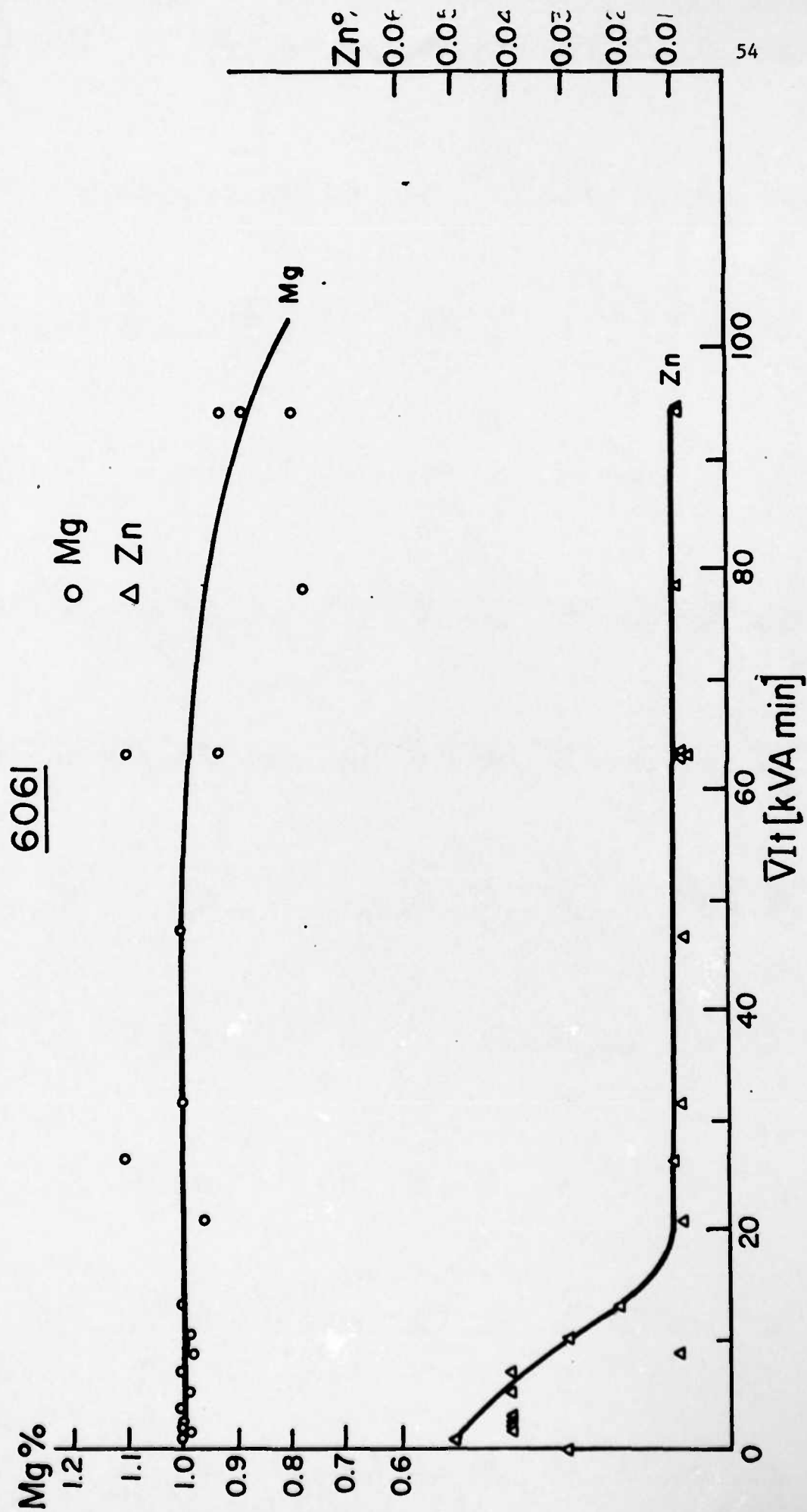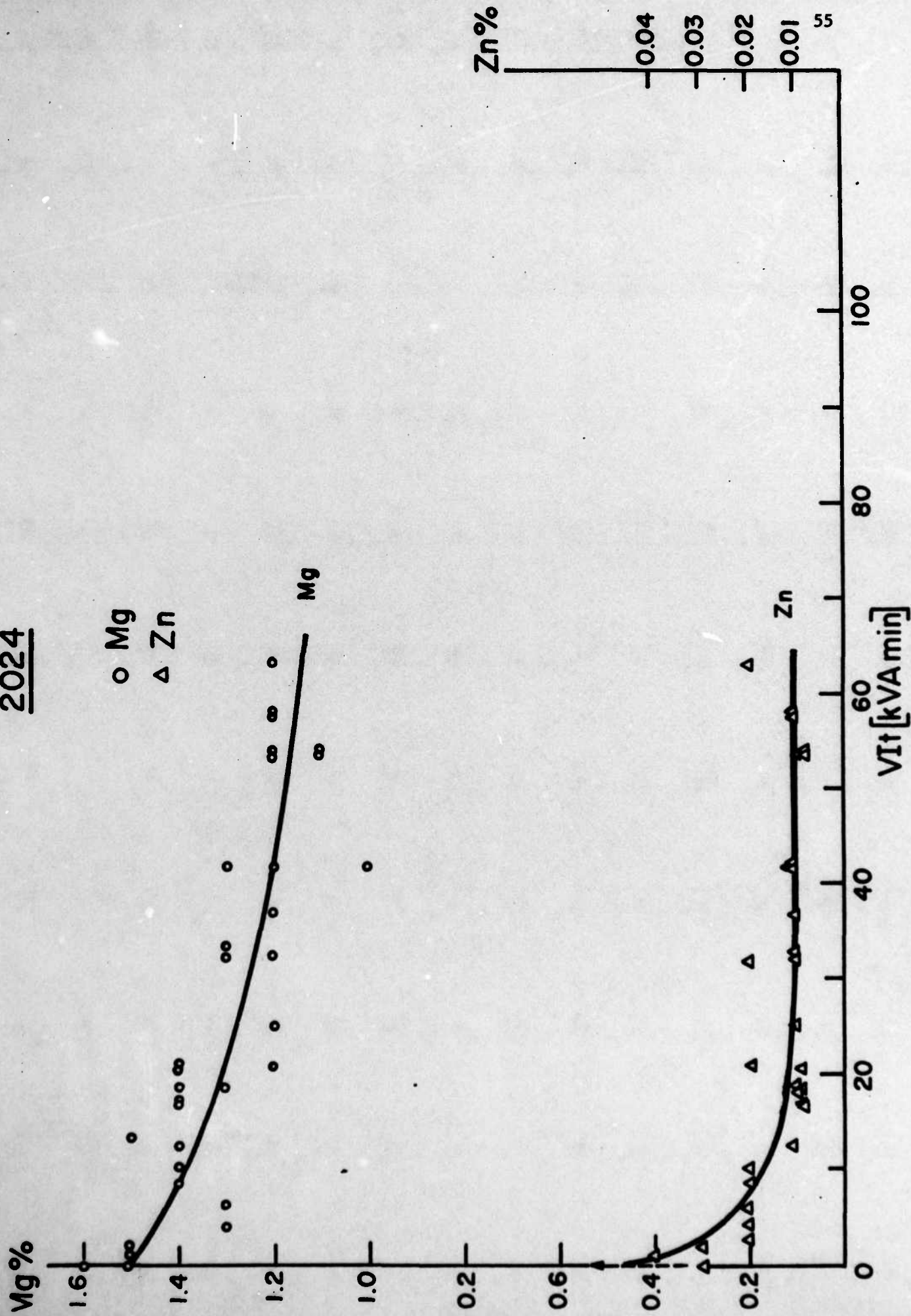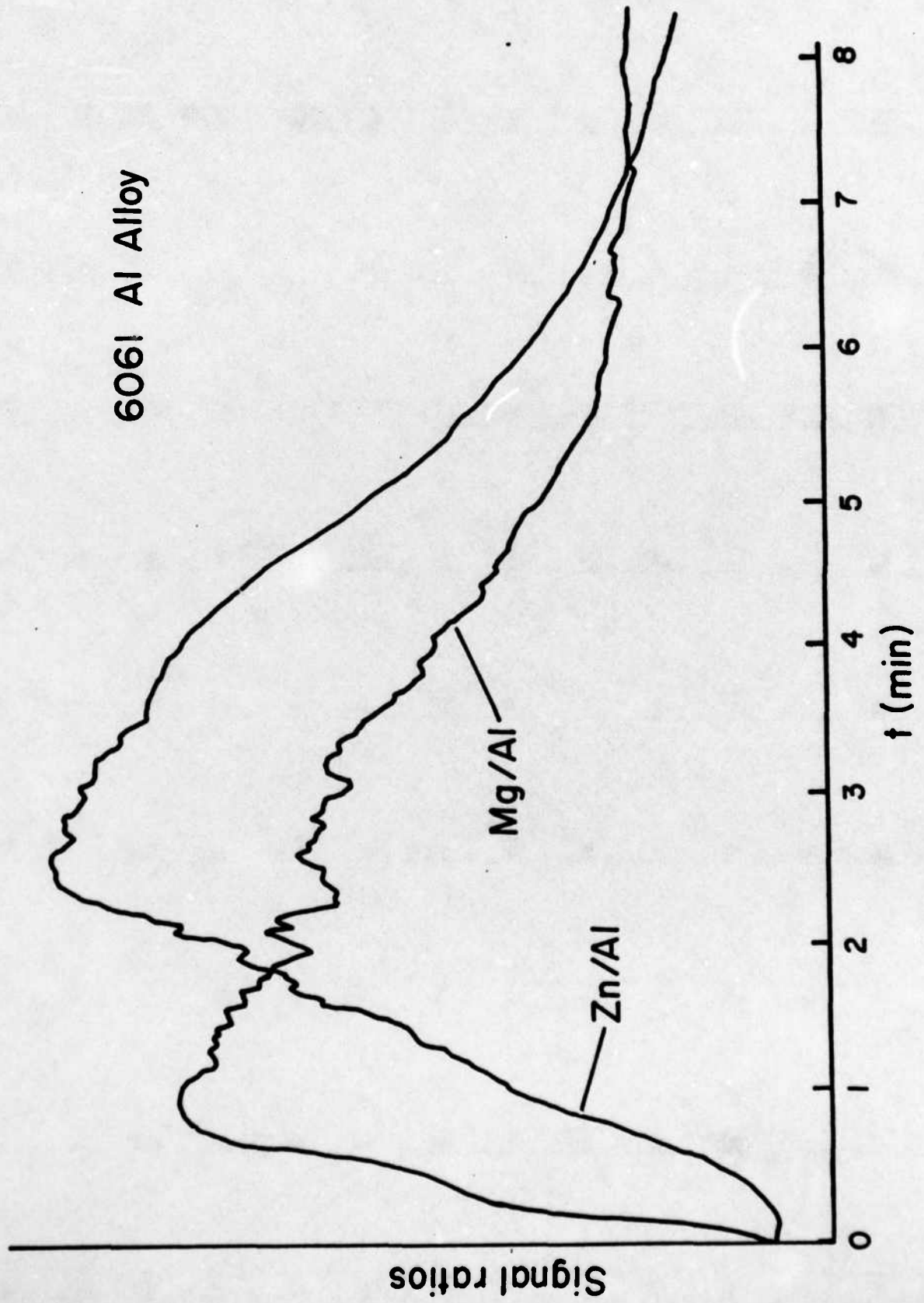
Gas Metal Arc Welding of Titanium

by

Daniel E. Ries

ABSTRACT

Gas Metal Arc (GMA) Welding of titanium was
investigated using an analog current regulator. The current
regulator has the capability of producing pulsed current
wave forms up to 25 kHz of practically any shape available
from a signal generator. The objective of this work was to
achieve control of metal transfer so that the molten filler
metal is incorporated into the weld pool in a controlled,
calm, orderly fashion. Normally, with DC current
conventional GMA processes, uncontrolled and unbalanced arc

forces tend to hamper controlled metal transfer when welding titanium. These unbalanced forces result in weld pool turbulance, uncontrolled droplet transfer and ultimately nonuniform weld bead formation and spatter. The use of rectangular pulsed current wave forms was investigated with respect to metal transfer control and ultimate weld bead shape uniformity.

An experimental space consisting of three independent variables including base current (I_b), peak current (I_p) and frequency (f), keeping the average current constant was investigated. Average current (I_{av}) was chosen based on the minimum DC level which produced a desired weld bead size. By changing the energy input at constant I_{av} using rectangular pulsed wave forms, changes in metal droplet transfer and resulting weld bead shape and uniformity were recorded. The experimental technique used for recording metal droplet transfer consisted of high speed photography (6,000 frames per second) using a balance of laser back lighting and arc illumination to record the size and frequency of formation of individual droplets. The current signal (high or low) was recorded on the film next to each high speed picture to allow real time analysis of droplet transfer as a function of pulsed current input. Data was taken using a multi-frequency level Box-Behnken design space grid allowing for statistical analysis of dependent

variables including weld bead width, wire feed rate, droplet transfer size, percent of droplet transfer rejected from weld pool as spatter, and droplet transfer frequency.

Thesis Supervisor: Thomas W. Eagar

Title: Associate Professor of Materials Engineering

A METHOD OF FILMING METAL TRANSFER IN WELDING ARCS

C. D. Allemand, R. Schoeder, D. E. Ries, and T. W. Eagar

Massachusetts Institute of Technology

Department of Materials Science and Engineering

Cambridge, Massachusetts 02139

INTRODUCTION AND PROBLEM DEFINITION

During studies of metal transfer in GMAW or SMAW it is often useful to perform high speed cinemaphotography of the transfer process; however, the high light emission from the arc creates a number of practical problems. The conventional solution is to flood the arc area with a light source of even greater intensity than the arc. This very intense light is then photographed through a very strong neutral density filter. While this approach provides a very good image of the metal transfer, the external light source is relatively expensive and the severe filtering of the arc light can result in loss of structural information about the arc plasma.

In this communication, an optical layout will be described, that has been used to take moving pictures of a filler wire and droplets in a gas

metal arc. More generally, the apparatus is applicable to observation of an opaque object surrounded by a bright and transparent light source of such high intensity that it blinds the detector and prohibits direct observation.

Initially an apparatus will be described which produces a shadowgram of the electrode and the detaching metal drops. Later, it will be shown that interchanging of a filter will permit a portion of the arc light to be transmitted, thus providing additional information about the arc plasma.

THE SHADOWGRAPH

The 0.8 mm diameter output beam of a 2 mW He Ne laser is expanded and spatially filtered into a 20 mm diameter collimated beam and used to illuminate the object represented in Figure 1 by an opaque sphere. Since the plasma surrounding the object is transparent at 633 nm, the collimated laser light passes through the plasma and is concentrated by lens 1 (placed at a distance of twice its focal length from the sphere) into the hole of a diaphragm placed at the focus of the lens. A narrow band interference filter which transmits at the laser wavelength is placed behind the diaphragm. All the laser light passes through this filter, except the part blocked by the opaque sphere and a small fraction which is absorbed by the filter. This simple apparatus may thus be used to form a shadowgram of the sphere. The image is produced at one focal length of lens q behind the diaphragm and is relayed to the high speed camera film plane by lens 2 of the camera.

To understand how the light from the arc is excluded from the

shadowgraph, one must remember that light from the arc is not collimated but is emitted in all directions. The arc light is not focussed on the diaphragm, and most of it is rejected at this point. The small portion of arc light that passes through the diaphragm (which acts as a spatial filter) is rejected by the narrow band interference filter. The arc light is nearly completely blocked by both the spatial and the wavelength filter, and only the laser light reaches the film to produce a red background with a sharp shadow of the object as seen in Figure 2.

The resolution of the image is limited by the diaphragm and by the quality of the imaging optics. Use of good quality 35 mm camera lenses and reasonably large diaphragm openings, (e.g. 1.5 to 3 mm), have produced acceptable resolution.

There are a number of considerations which make this system more practical:

1. The object on the first image plane is reversed such that the camera records an upside down picture. This is reversed by adding another lens (2, Figure 3) that produces a secondary, rightside up image. This lens can also be used as a relay lens to increase the distance from the object to the camera.

2. The camera lens diameter (4, Figure 3) is usually much smaller than the beam diameter at the level of the camera lens. Therefore, much of the field is lost; however, this may be restored to full object size by a field lens (3) placed on the second image plane.

3. The camera lens has a diaphragm that is normally used to adjust the film exposure. In the directed light system described, light from a point in the object area reaches a well defined and small part of

the camera lens. Therefore, the camera-lens-diaphragm does not act as a normal aperture stop but rather as a field stop. Since this is not wanted, the camera lens diaphragm should be kept wide open and the exposure is adjusted by means of neutral density filters. The exposure was measured roughly by means of a 35 mm still camera before test runs with the high speed camera were made. The aperture of the 35 mm camera was opened wider than the beam, and the focal length of its lens was taken into account to estimate the correct exposure for the high speed movie.

4. When studies are performed in a glove box, the laser beam can be introduced into and led out of the glove box through glass windows also shown in Figure 3. These windows should be polished plane parallel glass tilted about 5° from vertical to prevent a second surface reflection from following the main optical path.

ADDITION OF ARC LIGHT ILLUMINATION

The shadowgraph produces a black image on a red background; without information on the droplet surface or even of the arc itself. Some of this information can be retrieved if one removes the 633 nm laser filter, thus letting some of the arc light through the system. The balance between the laser and the arc light is reached by adjusting the diameter of the diaphragm hole and by adding a neutral density filter where the narrow band filter had been located. This produces an image of the electrode and droplets which is back-illuminated by the red laser light and front-illuminated by the blue arc light (Figure 4). The arc itself is clearly visible and can be allowed to overexpose as a white image on

the film. The instrumental parameters of this system are given in Table 1.

CONCLUSION

A method has been described which permits viewing of metal transfer in welding arcs using relatively inexpensive optical components and a small size He-Ne laser. In many cases, the optical information transferred by this method is superior to that obtained through use of intense external light sources and very dense neutral filters.

FIGURE CAPTIONS

Figure 1: Simplified optical diagram of the shadowgraph showing the way spatial and interference filters were used to block off arc light and admit laser light only. Note that in this diagram the laser beam overfills the camera lens. An opaque drop is shown in the object area and its shadow is traced to the film. The image position and height is indicated by the intersection of the image plane and the chief ray through the center of each imaging lens is represented by a dashed line.

Figure 2: 16 mm movie shadowgram obtained with the shadowgraph of Figure 1 in which a field lens has been added. The filler wire and a falling droplet are clearly visible but the arc is not recorded. The interference rings are partly due to the absence of a spatial filter in the beam expander and partly to the presence of a narrow band interference filter.

Figure 3: Complete optical layout. The interference filter has been removed to allow enough arc light through the optical train for the film to record the arc path. An erector lens and a field lens have been added. See text for details.

Figure 4: Gas metal arc welding of titanium: (a) Cathode plasma jet forms; (b) jet repels metal drop; (c) drop detaches, jet breaks; (d) jet broken. Replacement of the narrow band filter

with the neutral density filter provides more information on
the behavior of the plasma as well as the droplet detachment.

TABLE 1

Laser:	Spectra Physics, 2 mW He Ne Model 145-02
Expander with spatial filter:	Spindler & Hoyer 258 Model 038655
Lens 1:	f 150 mm, 6 elements, self-designed*
Neutral density filter:	ND 0.5, OPCO Labs, Leominster, MA
Erector lens:	Mamiya/Sekor 1:2/50
Diaphragm:	NRC Model 1D-1.5 opened 1.5 mm
Interference Filters:	633 nm, Andover Corp., Lawrence, MA
Field Lens:	f 200 mm bi-converse simple lens, 40 mm diameter
Camera Lens:	Schneider Tele-Xenar 1:2.8/75
Spacer Ring:	10 mm
Camera:	Redlake Hycam, model 41
Optical Benches and Accessories:	Klinger Scientific

---

* This lens may be replaced by a commercial f 150 mm photographic or reproduction lens with a clear aperture of 25 mm or more.
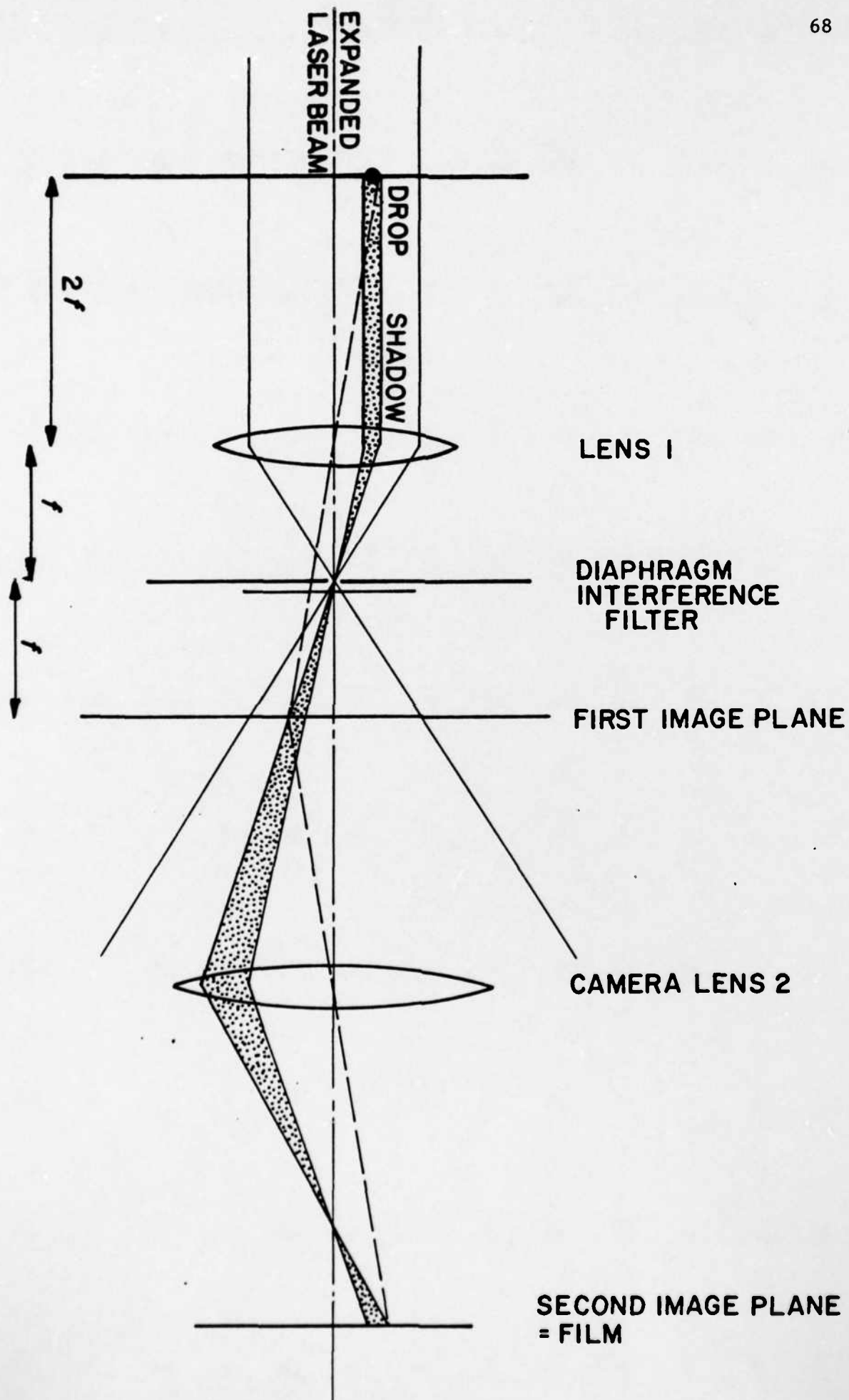
Fig. 1
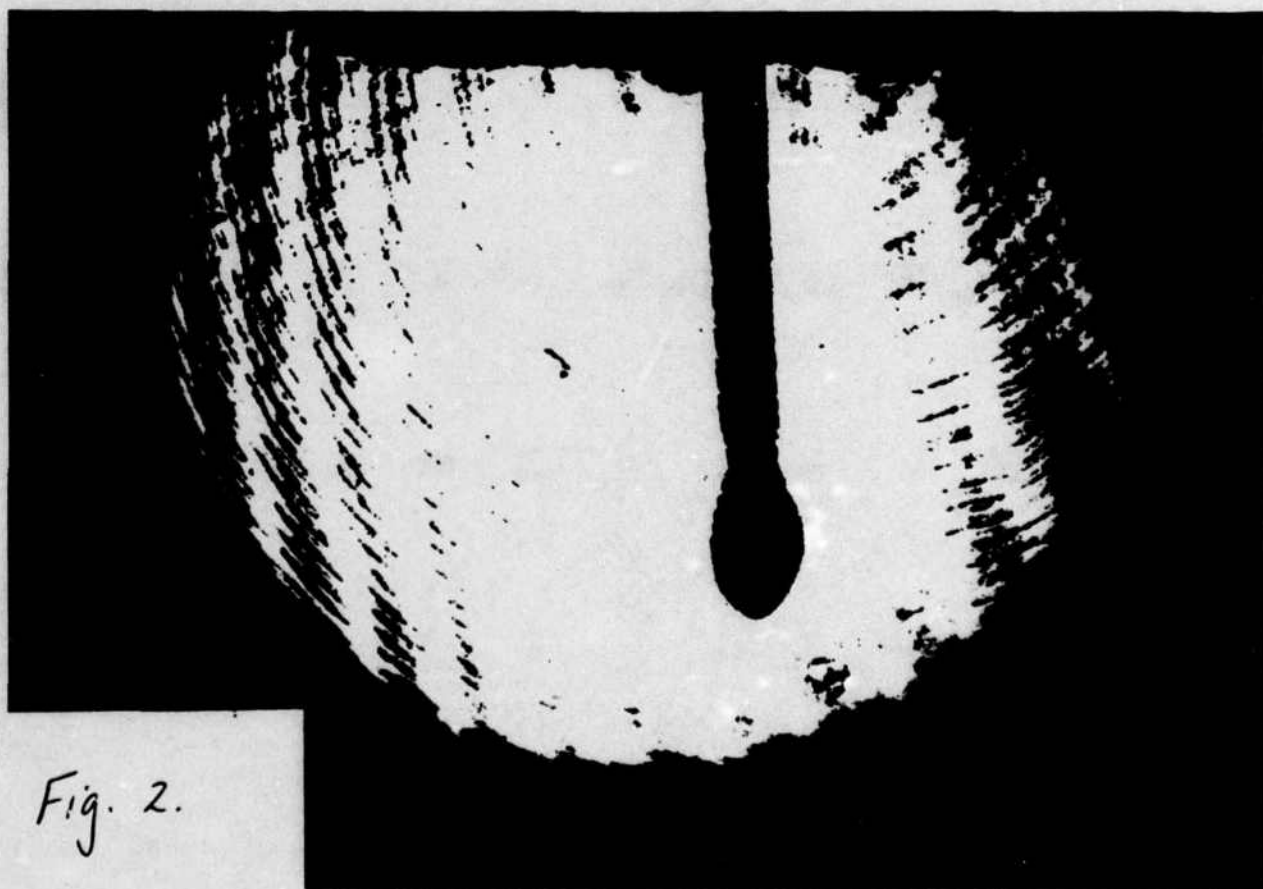
Fig. 2.
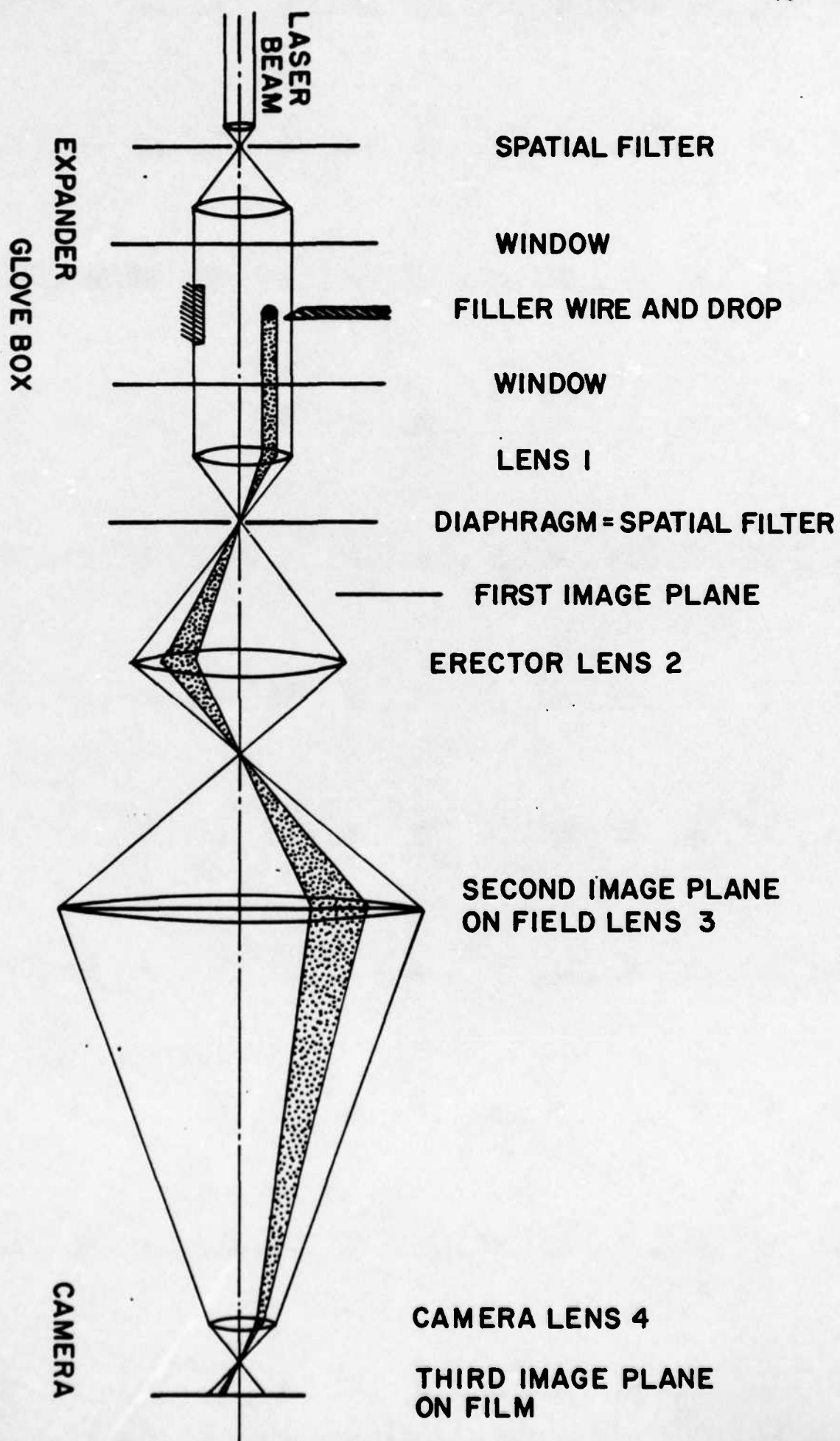
Fig 3

APPENDIX D

CONTACT TIP WEAR IN GAS-METAL ARC WELDING OF TITANIUM

by

Karl Thatcher Ulrich

Submitted to the Department of Mechanical Engineering
on January 27, 1984 in partial fulfillment of the
requirements for the degree of

Bachelor of Science

ABSTRACT

When titanium wire is used in gas-metal arc (GMA) welding, copper
contact tips wear more rapidly than when steel wire is used. This wear
is accompanied by arcing between the base plate and the contact tip
instead of between the plate and the filler wire, a phenomenon called
''burnback.'' Burnback requires a complete shutdown of the welding
operation and is therefore an expensive problem. Experiments were run
to understand the mechanism of contact tip failure. The results of
these experiments reveal that the low thermal conductivity of titanium
causes melting to occur at the sliding electrical contact junction
between the filler wire and the contact tip. Melting and subsequent
freezing of titanium at the contact point can either build up and cause
jamming of the filler wire in the contact tip or can cause adhesion of
a chunk of titanium to the filler wire that then abrades the copper
contact surface. The mechanism leading to the jamming of wire in the
contact tip led to burnback in several of the experimental cases.

Thesis Supervisor: Thomas W. Eagar
          Title: Associate Professor of Materials Engineering

APPENDIX E

METALLURGICAL FACTORS INFLUENCING

CHARPY ENERGY OF

SUBMERGED ARC WELDED

HY-80 STEEL

by

Adebisi O. Oladipupo

Submitted to the Department of
Materials Science and Engineering
on January 20, 1984
in partial fulfilment
of the requirements for the degree of
Master of Science in Materials Engineering.

ABSTRACT

Several metallurgical factors affecting charpy energy of submerged arc welded HY-80 Steel, have been investigated. The principal objective was to find an explanation for the mechanical response of the metal using different welding conditions. Correlations of the welding characteristics were made with microstructure, transformation behavior, content of interstitial solute, and net heat input. These studies indicated which factors may be important in optimising weld metal toughness of HY-80 steels.

In this study, three major microphases were observed :acicular ferrite, pro-eutectoid ferrite, and widmanstatten ferrite side plates. Acicular ferrite was found to be the most desirable of these three phases in improving weld metal toughness. It had a correlation coefficient of 0.954 with mean charpy value. Retained austenite which is a relatively minor phase (0.15%-2.4%) in the weld metal was also found to correlate very well with mean charpy value with a correlation coefficient of 0.80.

The effect of net heat input on charpy energy is indirect . Increasing heat input increases the ferrite vein spacing which in turn increases the amount of pro-eutectoid ferrite at the expense of acicular ferrite. A poor correlation (-0.185) of heat input was obtained with mean charpy value. In studying the transformation behavior of the welds, acicular ferrite was found to be the low transformation product and pro-eutectoid ferrite the high transformation product. However, the transformation temperature of the welds did not differ significantly in spite of the wide range of the mean charpy values. It was observed in this study, that nitrogen in weld metal can have deleterious effect on weld metal toughness even at low concentrations. (0.008-0.017%). A correlation coefficient of -0.571 was obtained with mean charpy value and

nitrogen content. This is believed to be significant considering the small measured nitrogen content of the weld metal.

Thesis Supervisor: Thomas W. Eagar
Title: Associate Professor of
Materials Engineering

APPENDIX F

(Presented at ASME Winter Annual Meeting,
Boston, MA, November 1983) ·

INFLUENCE OF SURFACE DEPRESSION AND CONVECTION ON
ARC WELD POOL GEOMETRY

M. L. Lin and T. W. Eagar
Materials Processing Center
Massachusetts Institute of Technology
Cambridge, Massachusetts

ABSTRACT

The relative importance of surface depression and convection in determining the depth of weld penetration in stationary GTA welds has been studied. The results indicate that a deep crater depression forms on the surface of a steel weld pool at currents in excess of 250 amperes. During the transition from shallow to deep penetration, the depression grows from one millimeter or less to four or five millimeters with an increase of only twenty amperes. Such a dramatic change cannot be explained due to the plasma jet momentum alone. It is proposed that the major cause of the deep penetration at these current levels is a vortex which is created by circumferential rotation of the weld pool. Some evidence suggests that the deep vortex is self-stabilizing and that this creates a hysteresis in the weld penetration as the current is ramped upward and downward through the transition from shallow to deep penetration. It is believed that this vortex depression is the major cause of "finger" penetration in GMA welding as well.

Travelling GTA welds were also made to investigate the effects of deep surface depression on weld defect formation. High speed cinemaphotography was used to show the flow behavior from the front to the back of the weld pool. In steels, and in titanium alloys, this flow is most likely driven by surface tension gradients. It was found that the deep vortex penetration and the rearward fluid flow can explain humped bead, undercutting and tunnel bead defects. It is believed that a similar mechanism is responsible for hollow bead defects in stovepipe welding.

INTRODUCTION

In order to improve productivity, more use is being made of automated welding; however, as a result, a number of problems arise which seldom occur in manual welding. Two of the most fundamental concerns are seam tracking and control of weld bead geometry, both of which must be controlled if a reliable weld is to be produced. In this paper several of the factors controlling weld bead geometry will be discussed. One of the difficulties encountered in a priori prediction of weld shape is that many parameters must be taken into account because all are found to have more or less influence on the weld pool geometry. If the welding process is to be automated with closed loop control of the weld zone size, it is desirable to more fully understand the mechanisms which influence heat and fluid flow in the molten weld pool so that the influence of these process parameters can be understood. Most of the fundamental research work on gas tungsten arc welding has been limited to low current ranges, i.e., less than about 200 amperes due to instabilities in the liquid pool and to the presence of defects such as humping and undercutting at higher currents. While good

agreement has been found between empirical data and the predicted values of weld pool geometry at low currents, when the current is increased to higher ranges, e.g., more than 250 amperes, more scatter is obtained. It is believed that surface depression and convective flow in the weld pool may begin to play important roles in these higher current regimes.

Rosenthal [1,2] first used point and line heat sources moving at a constant speed to calculate pure conduction heat transport in plates of semi-infinite thickness. Tsai [3] found that the inconsistency between the experimental weld pool shape and the predicted value based on the simple point source theory can be reduced to a large extent by assuming a distributed heat source on the weld surface. It was found that the introduction of the distributed heat source can match the predicted values of weld geometry reasonably well with the empirical data at low currents. At high currents, much larger errors are found, which suggest that effects other than thermal conduction and the distributed heat source may be important.

Generally, depression of the weld pool surface has received little attention. Ishizaki [4] studied depression in gas metal arc welds but no extensive study of surface depression in gas tungsten arc welding has been found in the literature. Most investigators believe that surface depression results from the impinging plasma jet. Such jets have been studied in steelmaking [5], however, these results can hardly be applied to the weld pool due to the large differences in dimension involved and to the fact that the equations derived are based upon empirical results in which the parameters are different from those in in gas tungsten arcs.

Numerous studies [6-12] have shown that the convective pattern in the weld pool influences heat flow and weld bead size. It is believed that the motive forces for fluid flow in the weld pool are (1) the electromagnetic force (Lorentz force), (2) the buoyancy force (thermal convection), (3) the surface tension force, and (4) the impinging gas jet force. There is little agreement as to which of these forces dominate under specified welding conditions; however, most authors agree that increasing the welding current is expected to increase the intensity of convective fluid flow because higher current density and heat flux will enhance the driving forces for fluid flow, which in turn will influence the penetration profile.

Fluid flow and surface depression are also responsible for the formation of weld defects such as humping and undercutting of the weld bead. Humping and undercutting are common in high travel speed and high current GTAW welding. The mechanisms of formation of these defects have been discussed by several researchers [7,13,14]; however, no satisfactory explanations have been proposed. Surface tension and arc force were mentioned as the forces which produce these defects, but the mechanisms are still poorly

understood. The purpose of the present paper is to assess the validity of previously explained mechanisms and to quantify the relative importance of surface depression and convection in determining the shape of arc weld pools.

EXPERIMENTAL PROCEDURES

A series of stationary and travelling bead-on-plate welds were made with varying currents, voltage and electrode tip angles. All the samples were cut from a single 304 stainless steel plate of 13 mm thickness. In stationary arc welding, measurements were made after a dwell time of 3 seconds so as not to overheat the plate. This time is long enough to approximate the heat input used in travelling arc welds. In order to see the influence of longer dwell time on the spot welding penetration profile, spots up to 24 seconds were also used. In travelling welds, a wide range of travelling velocity was used in order to investigate the effect of speed on the formation of weld defects and on the penetration mechanisms. Pure argon was used with the flow rate set at 1 m³/hr ± 10%.

Electrodes with 30, 60, 90, 120 degree cones were used. Welding current varied from 200 amperes to 350 amperes while arc voltage was set at three different values; 10V, 12V and 15V. In several tests, welding current was upsloped and downsloped in order to see a transition from shallow to deep penetration.

High speed photography was also used to investigate the fluid flow on the top surface of the liquid pool and to provide a clearer view of the sequence of formation of weld defects.

RESULTS

Stationary Arc Welds

As shown in Figures 1 and 2, a small increase of welding current can increase the surface depression of a spot weld by a large amount. The deep surface depression in high current ranges produces a finger-type penetration profile as shown in Figure 2. A cone-shaped
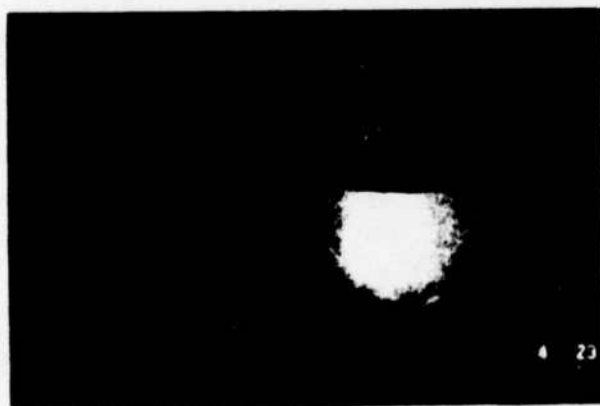

Fig 1(a) Surface depression and penetration profile at 235 amperes of a stationary arc weld on 304 stainless steel after three seconds.

cavity is often found at the bottom of these deep penetration profiles. For electrodes with larger tip angles such as 90 and 120 degrees, the "transition current" from negligible to significant surface depression depth is increased to slightly higher currents. This might suggest that plasma jets play an important role since such jets are stronger at low tip angles; however, this

matter will be discussed subsequently.

Fig. 1(b)
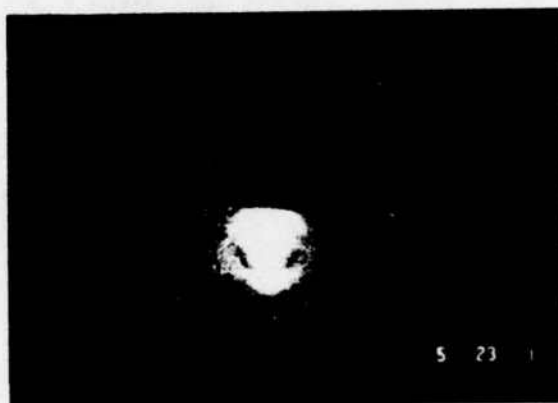
Fig. 2(a) Surface depression and penetration profile at 285 amperes of a stationary arc weld on 304 stainless steel after three seconds.

Fig. 2(b)

As shown in Figure 3, no increase of weld pool depth was found when welding time was increased from 3 seconds to 24 seconds; however, both the width and the area of the weld pool were found to increase with time.

Travelling Welds

Humping beads were found at high currents and at high travelling speed as shown in Figure 4. When the travel speed of the arc is less than 2 mm/sec., no humping is found and the weld pool shape does not
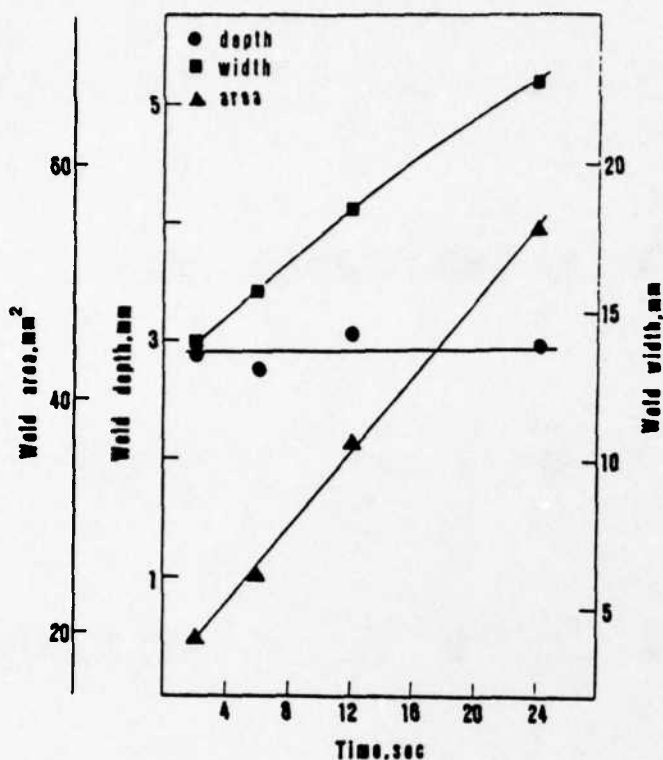
Fig. 3 Variation of weld depth, width and area with welding time for a stationary 285 ampere argon arc with a 30 degree electrode tip angle.

Fig. 5(a)

Fig. 5(b) Sequence of photos showing eddy motion behind the arc.

Fig. 4 Top view of humped welds.

differ from that observed in stationary arc welds. When the travel speed increases, humping begins to form. Figure 5 shows the motion of liquid metal before the hump forms. The growth of an eddy motion behind the arc is clearly seen. This eddy motion was also observed in high speed films. Occasionally, two eddies were seen behind the arc as shown schematically in Figure 12b.

Figure 6 shows the effect of varying current on the weld geometry. When the current increases from 250 amperes to 300 amperes, an abrupt increase of the penetration depth causes the formation of a tunnel cavity. At still higher currents, this cavity disappears. This disappearance is most likely due to a greater volume of liquid available in the 350 ampere weld. This large

Fig. 6 Variation of the longitudinal penetration contour with different maximum working current. Note: tunnel porosity is partially closed at the higher welding currents.

volume of liquid fills the cavity formed by the deep surface depression.

DISCUSSION

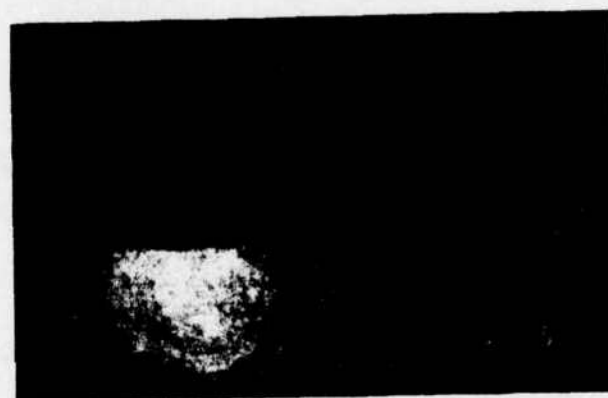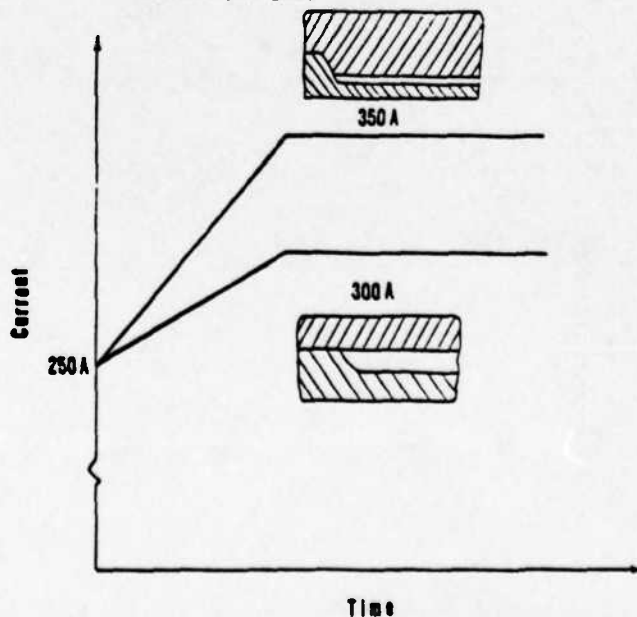It will be shown that previous models of weld convection are not capable of explaining the behavior noted above. In this paper a new model will be presented which way explain the observed behavior. The first problem to be considered is the abrupt transition from shallow to deep penetration as seen in Figures 1 and 2.

Compound Vortex

Usually the plasma jet force is mentioned as the cause of deep surface depression; however, if this is true, one would not expect an abrupt increase in depression within the transition current range as shown in Figure 6, since the plasma jet force increases in a smooth manner as the square of the arc current [15]. In addition, a simple analysis indicates that the plasma jet only has sufficient force to depress the pool by 1 mm at 300 amperes (see the Appendix). A possible mechanism which may explain the observed sudden increase of surface depression and the depth of the depression is a compound vortex as shown in Figure 7. Such a vortex can be developed at high welding currents due to a
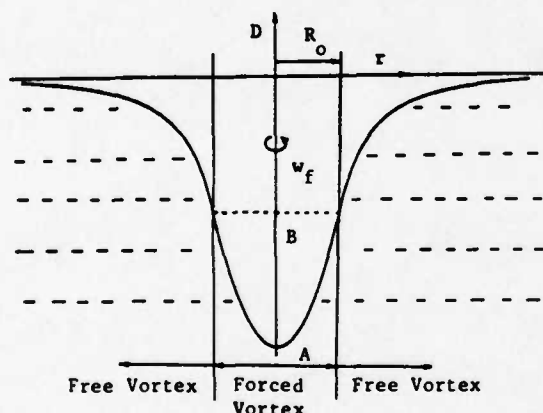

Fig. 7 Structure of the compound vortex. Assuming no transition region between the forced and free vortex.

circumferential rotation of the liquid. A compound vortex consists of a forced vortex in the central zone of the liquid pool together with a free vortex in the regions farther away from the central zone. The depth produced by a forced vortex in an infinite large liquid pool is

$$D = \frac{w_f^2 \gamma^2}{2g} \qquad \gamma \le R_o$$

with the origin referred to point A in Figure 7 and the depth produced by the free vortex in a similar pool is

$$D = \frac{w_f^2 R_o^4}{2g} \left(\frac{1}{R_o^2} - \frac{1}{\gamma^2} \right) \gamma \ge R_o$$

with the origin referred to point B in Figure 7 where w_f is the forced angular velocity in the forced vortex region, R_o is the radius of the forced vortex region and g is the acceleration of gravity.

Figures 8 and 9 show the calculated surface depression for different values of R_o and w_f. It can be seen that as the forced angular velocity w_f increases, the maximum surface depression depth increases sharply and the shape is similar to the observed finger-type depression. In addition, as R_o increases, the depth of finger-type surface depression also increases. This means that wider, higher current welds are more susceptible to formation of deep surface depression since R_o is greater. In addition, it will be noted that the vortex depression does not depend on the density of the metal, whereas metal density has a direct influence on surface depression caused by plasma jet forces. In practice, the deep depression is found to be no greater in aluminum than in steel. This agrees with the vortex model of depression whereas the plasma jet model predicts two to three times greater penetration in aluminum than in steel.
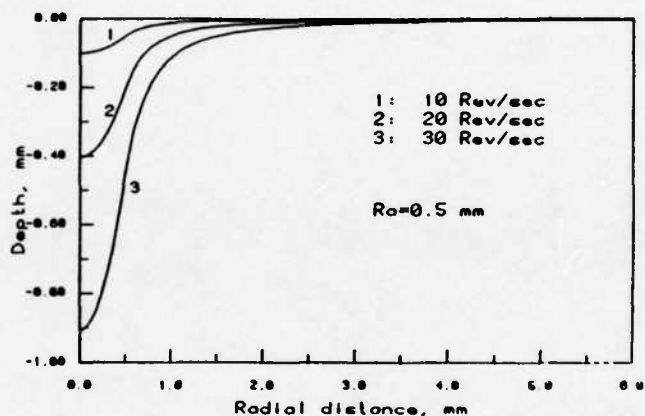
Fig. 8 Depth induced by compound vortex with a small forced vortex region R_o = 0.5 mm.

One might question the source of the circumferential flow which produces the vortex; however, the cause of this circumferential flow has been discussed by Millere et al. [16]. In essence, an arc perfectly aligned along the axis of symmetry cannot produce a circumferential flow, but any perturbation from the central axis is unstable and will grow until a circumferential flow is produced.
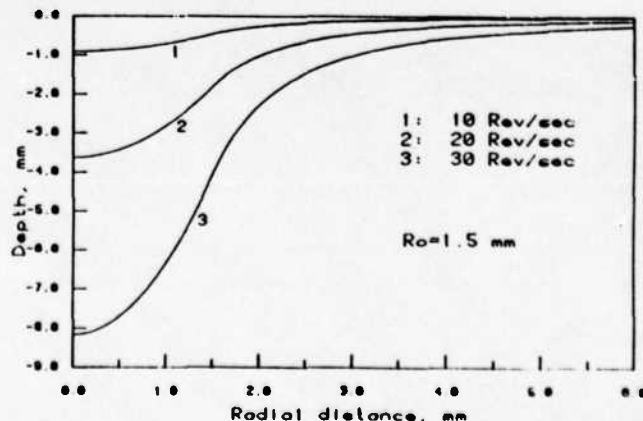

Fig. 9 Depth induced by compound vortex with a large forced vortex region R_o = 1.5 mm.

When the current is low, the plasma jet force is believed to be the dominant factor in determining the surface depression. As current increases, the vortex intensity increases. In the transition current ranges, in addition to the plasma jet force, the vortex may be strong enough to cause finger-type surface depression of the liquid puddle.

Heat Distribution in Arc Column at High Currents

In Figure 3, it is shown that the area and the width of weld increases with time while the depth of weld is nearly constant. This implies that the deep surface depression of the weld pool at high currents may greatly modify heat flow and current flow in the arc column, since the central region of the weld pool receives little heat from the arc column at high currents.

In the low current range, the gas-liquid interface is essentially planar and heat distribution in the arc can be approximated by a Gaussian distribution. However, in the high current range, a Gaussian distribution may no longer represent the true heat distribution. This maldistribution is caused by the deep surface depression of the anode surface, most of the current will flow to the side surfaces of the crater instead of being
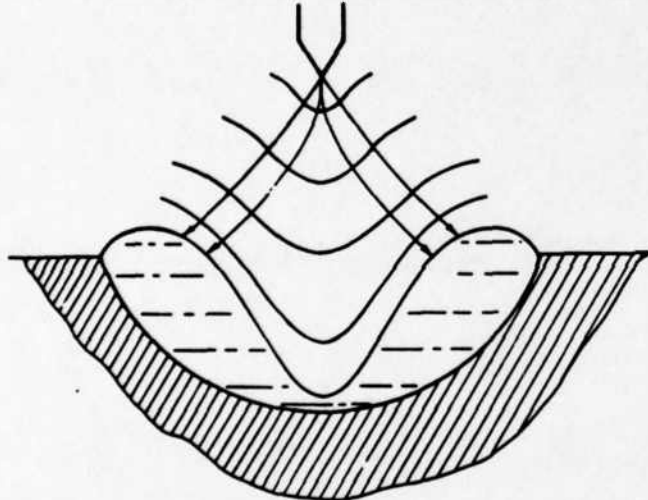

Fig. 10 Schematic representation of the equipotential lines and the current flow paths when a deep crater forms.

distributed evenly over the crater surface. This arises from the fact that both the cathode and the anode surfaces have constant electric potentials, therefore, the deep surface crater will make the equi-potential lines denser on the side surface than at the bottom of the crater. Thus, maldistribution of current flow is expected. Since 80 percent of the heat in the arc column is transported by the current, there is almost no heat transferred to the bottom of the crater, and the depth does not increase with time. Once the crater is formed, most of the current is deflected to the side walls of the crater, and it therefore requires less current to sustain the crater than is required to form the crater originally; thus a hysteresis loop in the penetration depth versus current graph occurs as shown in Figure 11.

The lack of heat transfer directly to the bottom of the crater has been observed in high speed cinema-photography and by metallographic sectioning, both of which show dry solid metal at the bottom of the crater. This also provides indirect confirmation of the vortex

theory, since a vortex and surface tension can extract all liquid from the bottom of the cavity whereas the plasma jet momentum would probably leave behind a thick film of liquid.

Defect Formation

Some of the mechanisms of defect formation at high currents can also be explained by deep surface depression and fluid flow in the liquid pool. As shown in Figure 12, at high welding currents, a deep surface crater is formed. As current enters the liquid metal, it will diverge. This divergence of current path causes a pressure gradient which induces fluid flow. Since the solid metal has higher electric conductivity than the liquid metal, most of the current entering the pool will flow to the front part of the arc, while less current passes through the elongated weld pool behind the arc as shown in Figure 12(b). The unbalanced distribution of current flow in the crater will usually push liquid metal forward as seen in Figure 12(b). However, surface tension forces push the liquid metal backward because the temperature in the front part of the arc is higher than behind the arc. Thus, in the initial stage of formation of humped weld beads, surface tension forces and electromagnetic forces compete to drive the liquid metal. In later stages, the liquid metal behind the arc becomes swollen, bringing it closer to the electrode and attracting more of the current to the liquid metal behind the arc. Finally, most of the current will flow to the humped weld bead behind the arc and the electromagnetic force will push the liquid metal backward in the same direction as surface tension forces. Thus, both the electromagnetic force and the metal is completely removed from beneath the arc. This unsteady motion can explain formation of humped weld beads.
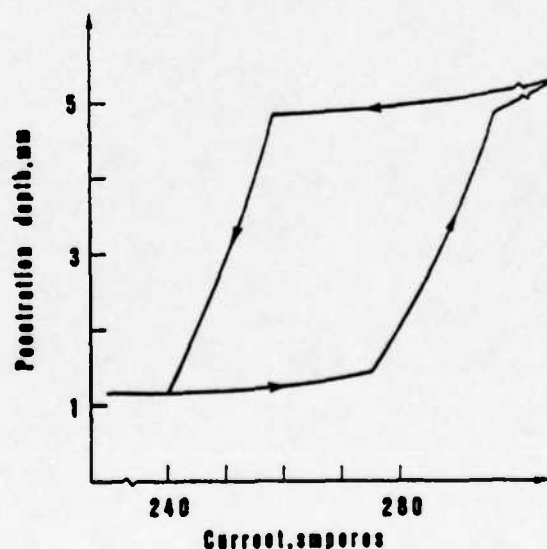
Fig. 11 Variation of penetration depth with current

Undercutting may also arise from convection in the weld pool. The eddy flows behind the arc will drive the liquid metal from the side surfaces of the groove by the travelling arc, to the centerline of the weld pool behind the arc. If the travel speed is great enough and hence the solidification rate is rapid enough, the liquid metal close to the centerline of the weld pool will solidify before this wave has time to reflect back toward the edges of the pool where the

liquid metal is depleted. The concentration of solidified metal along the centerline of the weld coupled with a depletion along the edges results in undercutting.

(a)

(b)
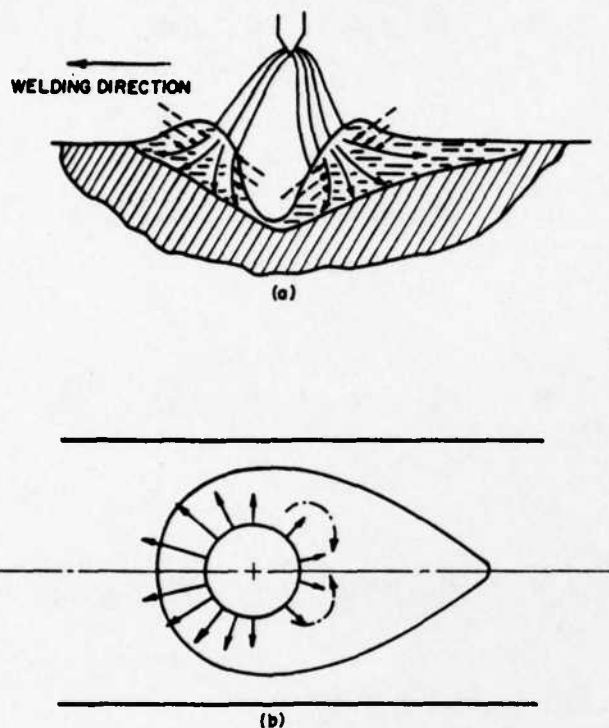
Fig. 12 Schematic representation of the formation of humping by maldistributed current in the liquid pool which produces unbalanced electromagnetic forces.

Finally, it is believed that the strong eddy motion behind the arc, as shown in Figure 12(b), is responsible for the tunnel bead defects shown in Figure 6. The eddy forms at the top of the plate with a depressed finger penetrating deeply into the metal. The circumferential eddy motion prevents metal from filling the bottom of the depression resulting in tunnel porosity along the base of the weld bead. It is believed that similar motion may account for the hollow bead defect noted in stovepipe welding. In this case, a deep depression or key hole is formed by the expanding gases produced by decomposition of the electrode coating. A circumferential flow may be induced which inhibits metal from "sinking" to the root of the weld bead in a manner similar to that described above for the tunnel porosity.

CONCLUSIONS

When the welding current is increased to a specific transition range, the depth of surface depression increases sharply in a manner that cannot be explained by plasma jet momentum alone. The formation of a vortex on the surface of the liquid pool may help explain both the magnitude and the form of this transition from shallow to deep penetration.

Deep surface depression and fluid flow may also explain the formation of a number of defects such as humped beads, undercutting and hollow beads. It is hoped that the greater understanding of the forces

described in this paper and the resulting convection in the weld pool may lead to improved methods of avoiding these problems in welded construction.

APPENDIX

Two approaches, a force balance and calculus of variation of the pool shape, were used to study the influence of plasma jet force on the depth of surface depression. The force balance in the case of an infinitely large liquid pool is

$$P_{arc} = \rho g h + \sigma \left(\frac{1}{R_1} + \frac{1}{R_2}\right)$$

ρ : density of liquid metal
h : depth of surface depression with respect to the highest point of depression curve
R_1, R_2: two principal radii of curvature of the surface at the centerline
σ : surface tension
P_{arc} : arc pressure

Using arc pressure data measured by Osaka Transformer Co. [17], one estimates a surface depression depth of 1 mm at 300 amperes and 90 degree electrode tip angle for values of $\sigma = 1300$ dyne/cm.

The shape of the surface depression which possesses the minimum energy given a constraint of a constant volume of the liquid metal can be calculated using calculus of variation. Using a computer to numerically solve this problem, it was found that, for a 90 degree electrode tip angle and pure argon shielding gas at 300 amperes, the maximum depth of surface depression is less than 1 mm [18]. Thus, both approaches show that plasma jet force cannot totally explain the magnitude of the surface depression nor can it explain the sudden increase of depression in the transition current range.

REFERENCES

1. Rosenthal, D., "Mathematical Theory of Heat Distribution During Welding and Cutting", Weld. J., 20(5), 1941, pp. 220s.

2. Rosenthal, D., "Theory of Moving Sources of Heat and Its Application to Metal Treatments", ASME, Vol. 68, No. 8, 1946, pp. 849.

3. Tsai, N. S., Ph.D. Thesis, Department of Materials Science and Engineering, Mass. Inst. of Technology, Cambridge, Mass., 1983.

4. Ishizaki, K., "A New Approach to the Mechanism of Penetration", Weld Pool Chemistry and Metallurgy, The Welding Institute International Conference, London, April 1980, pp. 65.

5. Bradshaw, A. V. and Wakelin, D., in "Heat and Mass Transfer in Process Metallurgy", The Institution of Mining and Metallurgy, London, 1967.

6. Apps, R. L., Milner, D. R., "A Note on the Behavior

of Liquid Metal Under the Arc", <u>Brit. Weld. J.</u>, Vol. 10, July 1963, pp. 348.

7. Bradstreet, B. J., "Effect of Surface Tension and Metal Flow on Weld Bead Formation", <u>Weld. J.</u>, Vol. 47, July 1968, pp. 314s.

8. Shercliff, J. F., "Fluid Motions Due to an Electric Current Source", <u>J. of Fluid Mechanics</u>, Part 2, Vol. 40, 1970, pp. 241.

9. Woods, R. A., Milner, D. R., "Motion in the Weld Pool in Arc Welding", <u>Weld. J.</u>, Vol. 50, April 1971, pp. 163s.

10. Lawson, W. H. S., Kerr, H. W., "Fluid Motion in GTA Weld Pool. Part 1, Flow Patterns and Weld Pool Homogeneity", <u>Welding Research Int'l.</u>, 6(5), 1976, pp. 63.

11. Bukarov, V. A., et al., "The Effect of Convection of Metal in the Weld Pool on Penetration", <u>Welding Production</u>, Vol. 25, No. 11, 1978, pp. 5.

12. Heiple, C. R., Roper, J. R., "Mechanicsm for Minor Element Effect on GTA Fusion Zone Geometry", <u>Weld. J.</u>, Vol. 61, April 1982, pp. 97s.

13. Paton, B. E., et al., "Certain Special Features of the Formation of Welds Made at High Speeds", <u>Auto. Welding,</u> Vol. 24, No. 8, 1971, pp. 1.

14. Savage, W. F., et al., "Effect of Arc Force on Defect Formation in GTA Welding", <u>Weld. J.</u>, Vol. 58, July 1979, pp. 212s.

15. Burleigh, T. D. and Eagar, T. W., Measurements of the Force Exerted by a Welding Arc", <u>Met. Trans.,</u> <u>14A(6)</u>, June 1983, pp. 1223-1224.

16. Millere, R. P., Sharamkin, V. I., and Scherbinin, E. V., "Effect of a Longitudinal Magnetic Field on Electrically Driven Rotational Flow in a Cylindrical Vessel", <u>Magnetohydrodynamics,</u> <u>16(1)</u>, 1980, pp. 66.

17. Unpublished technical report, Osaka Transformer Co., Osaka, Japan, 1980.

18. M. L. Lin, unpublished research, 1983.

APPENDIX G

INFLUENCE OF ARC PRESSURE ON WELD POOL GEOMETRY

M. L. Lin and T. W. Eagar
Materials Processing Center
Massachusetts Institute of Technology
Cambridge, MA 02139

ABSTRACT

At currents over 300 amperes, the surface of the weld pool becomes markedly depressed and the assumption of a flat surface is no longer valid. In order to predict the weld pool geometry, the shape of the surface depression under the action of the arc pressure has been calculated. At currents of 300 amperes, it is shown that the arc pressure cannot account for the experimentally observed deep surface depression. A compound vortex is proposed as a possible mechanism to explain the deep surface depression.

INTRODUCTION

A number of investigators have studied the magnitude of arc pressure in gas tungsten arcs(1-6). Some attempts have been made to explain the formation of several weld defects such as humped beads, finger penetration and undercutting(6,7,8) based on the asumption that the arc pressure depresses the surface of the weld pool. An analytical model was developed by Friedman(9) to simulate the distortion of fully penetrated molten pools in thin plates under the action of arc pressure and gravitational forces. In our own experiments, we have studied the influence of welding currents on the depth and shape of the surface depression(10). Surprisingly, it was found that the surface depression depth is

very small (less than 1 mm) at currents up to 240 amperes, but the depth increases rapidly as the current is increased by 30 amperes; see Figure 1. This rapid change in surface depression depth is difficult to explain by the increase in arc pressure which scales parabolically with weld current(11). In order to evaluate whether arc forces of the magnitudes measured previously(2) are capable of explaining the experimentally observed surface depression depths, an analytical model was developed. This model accounts for the balance of hydrostatic potential energy and surface energy with the work performed by the arc pressure displacing the liquid. The results of this model may be used to explain the experimental observations at low currents, but the results cannot explain the experimental evidence obtained at high currents. A simplified convection model is proposed which can in principle explain the very deep surface depression of the weld pool at high currents.

ANALYTICAL MODEL

The surface depression will form a shape which minimizes the total energy, hence, calculus of variation may be used to calculate this shape under the action of arc pressure subject to the constraint that the volume of the weld pool is constant. In this model, it is assumed that there is no convection in the molten pool.

The energy to be minimized is the surface energy plus the potential energy of the liquid pool. Analytically, this takes the form

$$J = \int_0^R \sigma \cdot 2\pi r \left[1 + (\frac{dw}{dr})^2 \right]^{1/2} dr + \int_0^R \rho g \cdot 2\pi r (h-w)(H - \frac{h+w}{2}) dr \qquad eq(1)$$

where the first integral on the right hand side of equation(1) is the interfacial energy between the gas and the liquid phase and the second integral is the potential energy of the liquid pool with respect to a reference plane at h=H. The geometry of this system is shown in Figure 2.

Equation(1) is subject to two constraints, firstly, constant liquid volume, which can be expressed as

$$\int_0^R G_1 dr = \int_0^R 2\pi r w \, dr = 0 \qquad eq(2)$$

where $G_1 = 2\pi r w$.

The second constraint requires that the work performed by the arc force be equal to the change of surface energy and potential energy of the liquid pool, however, the description of this constraint requires some discussion.

The first law of thermodynamics tells us that the energy of the system is conserved; however, the work performed by the arc force is not a state function but is path dependent. Consider the application of the arc pressure instantaneously. The volume of the liquid will be displaced by an amount ΔV and the work is $P\Delta V$; however this work is not reversible. The path of this form of work is given by ABC in Figure 3 and the work is the area ABCD. If on the other hand, one considers that the pressure is increased slowly and incrementally, the volumetric displacement of the

liquid might follow a path similar to AC in Figure 3. The work done in this case is given by the area ACD. This would be the reversible work. If we assume that the volumetric displacement changes proportionally to the increased pressure, the reversible work is one-half of the irreversible work of path ABC. Depending on the path chosen, the efficiency may vary from 0% to 100% for the conversion of work performed by the arc force to the change of surface energy and potential energy. Thus, another variable η is introduced to account for the efficiency of work conversion.

Accordingly, we may equate the work performed by the arc force to the change in surface energy and potential energy of the liquid pool by the following:

$$\int_0^R G_2 dr = \int_0^R G_3 dr + \int_0^R G_4 dr \qquad eq(3)$$

where $G_2 = \eta P_{arc} 2\pi rw$ and $\int_0^R G_2 dr$ is the fraction of work done by the arc force on the molten pool. The next term G_3 is given by

$$G_3 = \sigma 2\pi r \left[1 + \left(\frac{dw}{dr}\right)^2\right]^{1/2} - \sigma 2\pi r$$

where $\int_0^R G_3 dr$ is the difference of surface energy with and without surface depression of the molten pool, and finally

$$G_4 = \rho g 2\pi r (h-w)(H + \frac{h+w}{2}) - \rho g 2\pi r h (H - \frac{h}{2}) = \rho g 2\pi r (\frac{w^2}{2} - wH)$$

where $\int_0^R G_4 dr$ is the difference of potential energy with and

without surface depression of the molten pool.

Using eq(2), J can be simplified as

$$J = \int_0^R \sigma 2\pi r \left[1 + (\frac{dw}{dr})^2\right]^{1/2} dr + \int_0^R (Hh + \frac{w^2}{2} - \frac{h^2}{2}) dr$$

If we define $F = \sigma 2\pi r \left[1 + (\frac{dw}{dr})^2\right]^{1/2} + Hh + \frac{w^2}{2} - \frac{h^2}{2}$

then $J = \int_0^R F dr$

Again using eq(2), eq(3) can be reduced to

$$\int_0^R G_2 dr = \int_0^R G_3 dr + \int_0^R G_5 dr$$

where $G_5 = \rho g 2\pi r \frac{w^2}{2}$.

We now define

$$G_6 = G_2 - G_3 - G_5 = \eta P_{arc} 2\pi r - \sigma 2\pi r \left[1 + (\frac{dw}{dr})^2\right]^{1/2} + \sigma 2\pi - \rho g 2\pi r \frac{w^2}{2}$$

where $\int_0^R G_6 dr$ is the difference of work performed by the arc force and the total system energy which is the summation of potential energy and surface energy.

If one applies the Euler-Lagrangian criterion(12)

$$\frac{\partial}{\partial w}(F + \lambda_1 G_1 + \lambda_2 G_6) - \frac{\partial}{\partial r} \frac{\partial}{\partial(dw/dr)}(F + \lambda_1 G_1 + \lambda_2 G_6) = 0$$

where λ_1 and λ_2 are Lagrange multipliers; one has a function which must be minimized subject to the two constraints noted previously.

After manipulation, the result of the Euler-Lagrangian criterion is

$$\frac{dt}{dr} = \frac{(1+t^2)^{1/2}}{\sigma r(1-\lambda_1)} \left[\rho g r w + \lambda_1 r(\eta P_{arc} - \rho g w) + \lambda_2 r - (1-\lambda_1)(1+t^2)^{-1/2} \right.$$

$$\left. \cdot (\sigma t + r t \frac{d\sigma}{dr} - \sigma r \frac{t^2}{1+t^2}) \right] \qquad \text{eq(4)}$$

if one sets

$$t = \frac{dw}{dr}. \qquad \text{eq(5)}$$

There are two boundary conditions

$t = 0 \qquad$ at $r = 0$

due to symmetry about the centerline of the weld pool and

$w = 0 \qquad$ at $r = R$

since the liquid must be in contact with the solid surface.

A computer program was developed to evaluate λ_1 and λ_2. After evaluating λ_1 and λ_2 together with suitable boundary conditions and constraints, eq(4) and eq(5) are then solved simultaneously by the Runge-Kutta method(13).

PARAMETRIC ANALYSIS OF THE MODEL

In this model, there are five parameters which may be related to the welding process. These are

(1) the density of the molten metal, ρ

(2) the surface energy of the molten metal, σ

(3) the half width of the weld pool, R

(4) the arc pressure, P_{arc}

(5) the efficiency of work conversion, η

The shape of the liquid-solid boundary is not included in this model. This is reasonable if movement of the gas-liquid boundary is small compared to the dimension of weld pool. It may be argued from hydrostatics that the shape of the solid-liquid boundary will not influence the result provided the gas-liquid boundary does not impinge upon the solid-liquid boundary.

Steel and aluminum are chosen in this model with density equal to 7.84 g/cm^3 and 2.7 g/cm^3 respectively. For the distribution of surface energy of the molten pool, it is assumed that the temperature distribution on the top surface of the molten pool is as shown in Figure 4(a). The corresponding surface tension distributions are shown in Figure 4(b) and 4(c). Figure 4(b) is for pure iron while Figure 4(c) is for metal with high concentrations of surface active elements, e.g., sulfur. Even the magnitude of these temperature and surface tension distributions are not appropriate for aluminum; however, the main purpose of choosing these distributions is to investigate the effect of surface tension on the surface depression of a molten pool. Other results could be calculated for aluminum if accurate surface tension values were availsble. The half width of the weld pool is sssumed to range from 0.5 cm to 1 cm. The src pressure is taken from reference 2 as shown in Figure 5, using an src pressure st 300 ampere current. With higher currents, simple multiplication of the src pressure data from the 300 ampere curve is assumed. While this does not represent a physical reality, it may be sufficient

to study the influence of arc pressure on surface depression of the weld pool. Two values, 50% and 100%, are used to account for the efficiency of conversion of work done by the arc force to the change of surface energy and potential energy of the weld pool. The value of 100% corresponds to path ABC of Figure 3 while the value of 50% corresponds approximately to path AC.

RESULTS

The results of this model are shown in Figures 6 to 11. A more complete set of tabulated results are listed in Table 1. The maximum depth of surface depression of the molten pool varies from 0.49 mm to 38.178 mm; however, for reasonable pressures exerted by a 300 ampere arc, the maximum value is less than 1.3 mm for a 1 cm wide liquid steel puddle. This is much less than the experimentally observed value of over 4 mm(cf. Figure 1). A discussion of the effects of varying the input parameters follows:

(a) Density of molten metal

When the density of molten metal increases, the surface depression depth is reduced as shown in Figures 6 to 11. The effect of density becomes more prominent when the top surface of weld pool becomes deeper. In Figure 6, the maximum depth of surface depression for steel is 0.49 mm and for aluminum the maximum depth of surface depression is 0.642 mm, hence, reducing the density by nearly a factor of three increases the depression by only 30 percent. However, at higher arc pressures, as seen in Figure 10, low density liquid has a maximum depth 160 percent larger than

that of the heavy liquid.

(b) Surface tension

The effect of surface tension on the depth of surface depression of the weld pool is shown in Figures 6 to 8. For the assumed surface tension distributions, type I and type II, as shown in Figure 4(b) and 4(c), the effect of surface tension on the shape of surface depression is not very important in both the low and the high surface depression ranges. The maximum surface depression depth is found to vary only 20% for high density metal and 40% for low density metal due to these different surface tension distributions.

(c) Width of weld pool

The effect of weld pool width can be seen in Figure 9 or by comparison of Figure 6 and 7. When the width of the weld pool increases, the surface depression depth also increases. This seems reasonable as long as the width of the weld pool does not extend beyond the region of the arc plasma. As can be seen in Figure 9, when the surface depression depth is small, the maximum depth increases only 80% when the weld pool width increases from 10 mm to 20 mm. However, when the surface depression depth is large, the maximum depth increases 140% when the weld pool width increases from 10 mm to 20 mm.

(d) Arc pressure

The arc pressure at 300 amperes causes a shallow depression (less than 2 mm), however; when the arc pressure is very high as shown in Figure 10 and 11, the surface dpression becomes very

large. This may imply that at higher currents, the depth of surface depression is dominated by the strong arc pressure. It should be noted that if the pressure distribution remains fixed in size but increases parabolically with current, the pressures of 2, 4 and 6 times the measured pressure at 300 amperes would correspond to currents of 425, 600 and 735 amperes respectively.

(e) Work conversion

The maximum depth of surface depression of irreversible work conversion is found to be approximately two times larger than that of reversible work conversion, as shown in Figure 9 and 11, which is perhaps not very surprising.

DISCUSSION

Experimentally, it has been observed that the surface depression at currents below 200 amperes is negligible, however; when current increases to about 300 amperes, a deep surface depression is found as shown in Figure 12. The maximum depth of surface depression is about 4.5 mm. From the model of the arc pressure, it is seen that the arc pressure cannot explain the deep surface depression at 300 ampere current, since the maximum depth of surface depression which was calculated for steel is 1.28 mm. This is much smaller than the actual depth of surface depression which is experimentally found to be 4.5 mm. Thus, some other mechanism must be responsible for the deep surface depression at these higher currents.

A compound vortex model is proposed to account for the deep

surface depression at high currents. A compound vortex consists of a forced vortex in the central part of the liquid pool with a free vortex surrounding the forced vortex. This is shown schematically in Figure 13. The result of the compound vortex model is shown in Figure 14. It can be seen that the depth of surface depression caused by the compound vortex is very close to the actual depth of the surface depression at high currents. This circumferential flow may come from the toroidal flow on the plane parallel to the arc axis. Millere(14) found that in an electrically driven rotational flow, the circumferential rotational motion on the plane normal to the arc axis increases with the intensity of electrovortex on the plane parallel to the arc axis. Therefore, part of the kinetic energy of toroidal flow on the plane parallel to the arc axis is transferred to the rotational motion, inducing the circumferential flow on the plane normal to the arc axis. It should be noted that the rotational velocities assumed in Figure 14 are less than one third of the velocities noted by Heiple and Roper(15) using high speed cinemaphotography; hence, these assumed rotational speeds are not thought to be excessive.

As a result of this study, three-current ranges may be proposed to explain surface depression of weld pools. At low currents (below about 200 amperes), the weld pool depression is shallow and does not significantly influence the shape of the weld pool. At higher currents (from about 300 amperes to 500 amperes), the surface depression greatly influences the weld pool geometry.

A circumferential vortex flow may be responsible for the formation of this surface depression and the presence of the 'finger' penetration seen in gas tungsten arc spot welds, GMAW and SAW beads. At even higher currents (above about 500 amperes), the arc pressure is strong enough that it may explain much of the deep surface depression which, in turn, influences the weld pool geometry. The three-current ranges proposed in this model are consistent with the results of Chihoski(16) who found four distinct current ranges for the depth of penetration in aluminum welds. In his study, the penetration shows a very slow increase with current in the 100-200 ampere range followed by a steep increase with current in the 200-300 ampere range. The 300-400 ampere range shows almost no response of current to penetration, but in the 450-600 ampere range, penetration begins to increase moderately with current.

Chihoski's 100-200 ampere range corresponds to the regime where surface depression is not significant. The 200-300 ampere range corresponds to the transition from little surface depression to formation of a full vortex, while the 300-400 ampere range corresponds to bottoming out of the vortex depression at the solid boundary. In such a case, the current from the arc, or the heat, follows paths normal to the isopotential lines in the plasma and hence is concentrated at the top edges of the liquid vortex and direct arc heat does not reach the bottom of the vortex, as shown in Figure 15. Above 450 amperes, the arc pressure becomes significant and together with the vortex, deepens the depression as the current is increased.

CONCLUSIONS

The depth of surface depression caused by the arc pressure distribtuion has been calculated using calculus of variations with suitable constraints. The results show that arc pressure only influences weld pool geometry at currents in excess of 500 amperes. At intermediate currents, the shape of the pool may be influenced markedly by circumferential convection. This flow may be responsible for the characteristic finger penetration of many weld pools. At even higher currents, arc force may become important and may have a significant influence on weld pool geometry.

ACKNOWLEDGEMENTS

The authors are grateful for support of this work by the office of Naval Research under Contract N00014-C-80-0384.

APPENDIX

Referring to Figure 13, the depth produced by a compound vortex may be estimated as follows:

In the forced vortex region,

$$D_1 = \frac{\omega_f^2 r^2}{2g}$$

with the origin referred to point A in Figure 15.

In the free vortex region,

$$D_2 = \frac{\omega_f^2 R_o^4}{2g} \left(\frac{1}{R_o^2} + \frac{1}{r^2} \right)$$

with the origin referred to point B in Figure 15.

The total depression is $D_1 + D_2$.

LIST OF SYMBOLS

T : temperature on the surface of weld pool($^\circ$C)

J : total system energy(erg)

σ : surface energy(erg/cm^2)

ρ : density of liquid metal(g/cm^3)

g : gravitational acceleration(cm/sec^2)

h : ordinate of solid-liquid boundary(cm)

w : ordinate of liquid-gas boundary(cm)

r : radial coordinate of weld pool(cm)

H : maximum depth of liquid pool(cm)

R : radius of the top surface of liquid pool(cm)

η : percentage of work conversion(%)

D : depth of liquid pool produced by a compound vortex(cm)

R_e : radius of forced vortex region(cm)

ω_f : angular velocity of the rotational motion

in forced vortex region(rad/sec)

TABLE I
Calculated maximum depth of surface depression

material	half width (mm)	* arc pressure	surface tension	work conversion	max. depth of surface depression (mm)
steel	5	1X	type I	rev.	0.490
steel	5	1X	type II	rev.	0.600
aluminum	5	1X	type I	rev.	0.642
aluminum	5	1X	type II	rev.	0.903
steel	10	1X	type I	rev.	0.893
steel	10	1X	type II	rev.	1.029
aluminum	10	1X	type I	rev.	1.511
aluminum	10	1X	type II	rev.	1.975
steel	5	1X	type I	irrev.	1.000
steel	5	1X	type II	irrev.	1.282
aluminum	5	1X	type I	irrev.	1.354
aluminum	5	1X	type II	irrev.	1.938
steel	10	1X	type I	irrev.	1.846
steel	10	1X	type II	irrev.	2.127
aluminum	10	1X	type I	irrev.	3.237
aluminum	10	1X	type II	irrev.	4.210
steel	5	2X	type I	rev.	1.000
steel	5	2X	type II	rev.	1.279
aluminum	5	2X	type I	rev.	1.354
aluminum	5	2X	type II	rev.	1.938
steel	10	2X	type I	rev.	1.857
steel	10	2X	type II	rev.	2.132

aluminum	10	2X	type I	rev.	3.235
aluminum	10	2X	type II	rev.	4.212
steel	10	6X	type I	irrev.	13.162
steel	10	6X	type II	irrev.	14.731
aluminum	10	6X	type I	irrev.	31.939
aluminum	10	6X	type II	irrev.	38.178
steel	5	2X	type I	irrev.	2.150
steel	5	2X	type II	irrev.	2.712
aluminum	5	2X	type I	irrev.	3.069
aluminum	5	2X	type II	irrev.	4.650
steel	10	6X	type II	rev.	6.821
aluminum	10	6X	type II	rev.	15.572
aluminum	5	4X	type II	rev.	4.641
aluminum	10	4X	type II	rev.	9.372
steel	7.5	1X	type I	rev.	0.741
aluminum	7.5	1X	type I	rev.	1.142

* This represents magnification of the 300 ampere arc pressure data given in Figure 5.